JGR Atmospheres

RESEARCH ARTICLE
10.1029/2021JD036296

# Experimental Determination of the Relationship Between Organic Aerosol Viscosity and Ice Nucleation at Upper Free Tropospheric Conditions

**Sabin Kasparoglu[1], Russell Perkins[2], Paul J. Ziemann[3], Paul J. DeMott[2], Sonia M. Kreidenweis[2], Zachary Finewax[3,4], Benjamin L. Deming[3], Marla P. DeVault[3], and Markus D. Petters[1]**

[1]Department of Marine, Earth, and Atmospheric Sciences, NC State University, Raleigh, NC, USA, [2]Department of Atmospheric Science, Colorado State University, Fort Collins, CO, USA, [3]University of Colorado Boulder, Boulder, CO, USA, [4]Now at NOAA Chemical Sciences Laboratory, Boulder, CO, USA

**Key Points:**

- Glass transition of terpene-derived secondary organic material ranges between 6 and 23°C. Carene-derived aerosol did not plasticize below −10°C at 120 s residence time
- No heterogeneous ice nucleation was observed for secondary organic material generated from terpene and aromatic precursors
- The presence of $ONO_2$ moieties or of close structural matches between known organic ice nucleating particles and products did not promote freezing

**Correspondence to:**
M. D. Petters,
mdpetter@ncsu.edu

**Citation:**
Kasparoglu, S., Perkins, R., Ziemann, P. J., DeMott, P. J., Kreidenweis, S. M., Finewax, Z., et al. (2022). Experimental determination of the relationship between organic aerosol viscosity and ice nucleation at upper free tropospheric conditions. *Journal of Geophysical Research: Atmospheres*, *127*, e2021JD036296. https://doi.org/10.1029/2021JD036296

Received 2 DEC 2021
Accepted 24 JUL 2022

© 2022. The Authors.
This is an open access article under the terms of the Creative Commons Attribution-NonCommercial-NoDerivs License, which permits use and distribution in any medium, provided the original work is properly cited, the use is non-commercial and no modifications or adaptations are made.

**Abstract** This work presents measurements of the ice nucleating ability of secondary organic material recorded between −40 and −70°C and relative humidity with respect to ice ($RH_{ice}$) between 150% and 220%. For a subset of systems, temperature and humidity dependence of particle viscosity as well as dry glass transition temperature were characterized using the dual tandem differential mobility analyzer method. Eleven unique monoterpene, sesquiterpene and aromatic precursors were used to generate secondary organic material (SOM) using either an oxidation flow reactor (OFR) or an environmental chamber (EC). For the SOM for which viscosity was measured, the particle glass transition temperatures varied between 6 and 23°C ($n = 8$). Measurements were performed to verify that increased relative humidity did not plasticize the particles below −10°C at residence times similar to those in the ice nucleation instrument. No heterogeneous ice nucleation was observed at the ~0.5% onset threshold for any of the materials generated. The ice nucleation occurs by the freezing of SOM solution droplets consistent with homogeneous freezing indicating that they form an aqueous solution, or the SOM particles required water saturation to freeze, indicating that they were hydrophobic. Experiments exploring the influence of functional groups and mass loading did not reveal any obvious influence of particle chemistry or generation conditions on the results. Close structural matches between known organic ice nucleating particles as precursor or formed products did not yield materials that promoted freezing. These experiments suggest that heterogeneous ice formation of glassy secondary organic materials is likely uncommon under upper free tropospheric conditions.

## 1. Introduction

Cirrus clouds play an important role in Earth's energy budget by reflecting the incoming solar radiation into space which leads to cooling, and by reducing the infrared longwave coming from the Earth surface which leads to warming (Chen et al., 2000; Heymsfield et al., 2017; Storelvmo & Herger, 2014). The radiative properties of cirrus clouds depend on the ice crystal number concentration, which in turn depends on the aerosol that nucleate ice at these conditions. Cirrus cloud ice crystals form either through homogeneous processes, requiring no ice nucleating particle (INP) or active site, or heterogeneously where an INP is involved (Hoose & Möhler, 2012; Kanji et al., 2017; Vali et al., 2015). Heterogeneous ice nucleation (IN) can occur via deposition of ice on particle surfaces, condensation in pores and subsequent freezing (Campbell et al., 2017; David et al., 2019; Marcolli, 2014), through immersion freezing of droplets as they cool, or condensation freezing as particles simultaneously uptake water and cool. Another freezing path is contact freezing where a particle approaches the air-water interface from either the outside of the droplet or from inside of the droplet (Durant & Shaw, 2005; Kanji et al., 2017). Homogeneous freezing of liquid aerosol is predominantly controlled by water activity (or ambient relative humidity (RH)), temperature, particle size, and hygroscopicity (Baumgartner et al., 2022; Koop et al., 2000; Schneider et al., 2021). Among these, temperature and RH dominate. Chemical composition influences homogeneous IN by modulating hygroscopicity (Junge, 1953; M. D. Petters & Kreidenweis, 2007). However, the overall influence of chemical composition on homogeneous freezing nucleation is small (Kreidenweis et al., 2009). In contrast, heterogeneous IN strongly depends on the chemical composition and morphology (Hiranuma et al., 2014). Ambient measurements of cirrus ice crystal residuals show a wide range of chemical composition, including organic particles, black carbon, mineral dust, lead and other metal bearing particles, sulfate particles, and salt particles

(Chen et al., 1998; Cziczo & Froyd, 2014; Cziczo et al., 2017; DeMott et al., 2003; Twohy & Poellot, 2005). Fewer heterogeneous ice nucleating particles result in conditions that are less conducive to cirrus cloud formation. In case cirrus clouds do form, they will have higher ice crystal number concentration when compared to air masses with higher ice nucleating particles concentration (DeMott et al., 2010). Identifying the particle properties that are conducive to ice formation is thus important for understanding the influence of aerosols on cirrus clouds and climate.

Many model organic species have been identified as IN active substances (Baustian et al., 2013; Gavish et al., 1990; Kilchhofer et al., 2021; Knopf et al., 2018; Murray et al., 2010; Rosinski et al., 1990; Wagner et al., 2010; Wolf et al., 2020). The reported observations show that particles composed of pure organic compounds such as sucrose (Baustian et al., 2013), raffinose (Kilchhofer et al., 2021; Wagner et al., 2012; Wilson et al., 2012), citric acid (Murray et al., 2010), and oxalic acid dihydrate (Wagner et al., 2010) nucleate ice in the heterogeneous regime. Deposition ice nucleation requires low ice supersaturation and temperature values which exclude haze particle or liquid droplet formation and homogeneous freezing. In addition to molecular composition, the trajectory of the particle along a thermodynamic path, and the glass transition temperature ($T_g$), which is non-equilibrium phase transition temperature from glassy solid-phase to semi-solid phase (Koop et al., 2011), are important modulators of the ice nucleating ability of a particle (e.g., Berkemeier et al., 2014; Charnawskas et al., 2017; Kilchhofer et al., 2021; Lienhard et al., 2015; Murray et al., 2010). When the glassy particle is exposed to an increase of RH, it starts to liquefy and form a core-shell morphology then the water diffuses into the glassy matrix. It leads to a full deliquescence of the particle, and this produces a transition from a glassy phase to a semi-solid or liquid phase of the particle (Berkemeier et al., 2014). Heterogeneous processes govern freezing until the particle is fully deliquesced. Homogeneous freezing occurs when the particle is fully deliquesced (Kanji et al., 2017). The aerosol water content and the associated semi-solid particle viscosity that is required to deactivate ice active organic surfaces remains unknown.

Atmospheric aerosols contain secondary organic materials (SOM) that form from the oxidation of volatile organic compounds, followed by condensation into the condensed phase (Hallquist et al., 2009). A number of studies investigated the potential influence of SOM on heterogeneous IN. Some authors suggest that SOM may nucleate ice heterogeneously. For example, Wang et al. (2012) report heterogeneous ice nucleation of SOM derived from OH oxidation of naphthalene between −45 and −70°C. Ignatius et al. (2016) show that viscous SOM formed from ozonolysis of α-pinene may nucleate ice heterogeneously at $T \approx -40$°C. Wolf et al. (2020) show that a small fraction of particles representing pure components of isoprene-derived SOM compounds nucleate ice heterogeneously at −46°C. However, several other studies have found that pure SOM (Charnawskas et al., 2017; Ladino et al., 2014; Piedehierro et al., 2021; Prenni et al., 2009; Wagner et al., 2017; Wolf et al., 2020) and particles coated with SOM (Koehler et al., 2010; Möhler et al., 2008; Zhang et al., 2020) require water saturation either consistent with homogeneous nucleation of haze droplets or higher to nucleate ice.

Explanations of the observed differences in IN behavior for SOM remain elusive. Viscosity and water solvation prior to reaching temperature and ice supersaturation are often cited as the key controlling factors that explain the difference in observed IN activity (Berkemeier et al., 2014; Reid et al., 2018). Previous studies relied on estimating viscosity and $T_g$ through modeling approaches. Here we combine direct observations of aerosol viscosity with ice nucleating activity at cirrus temperatures. We report IN measurements of SOM formed from the oxidation of terpene (monoterpene and sesquiterpenes) and aromatic precursors at temperatures below −40°C, that is, below the homogeneous freezing temperature of pure water. SOM was generated using either an oxidation flow reactor (OFR) or an EC. Temperature and humidity dependent viscosity and volatility were measured using the dimer coagulation and coalescence method and a volatility tandem differential mobility (DMA) analyzer for a subset of systems. Volatility was measured to serve as a proxy for viscosity since volatility has been reported to correlate with viscosity (Champion et al., 2019; Li et al., 2020).

## 2. Methods

The overall experimental set up is given in Figure 1. The experiments include setups for (1) particle generation, (2) viscosity measurement, (3) volatility measurement, (4) size distribution measurement, and (5) IN measurement. These are now discussed sequentially.

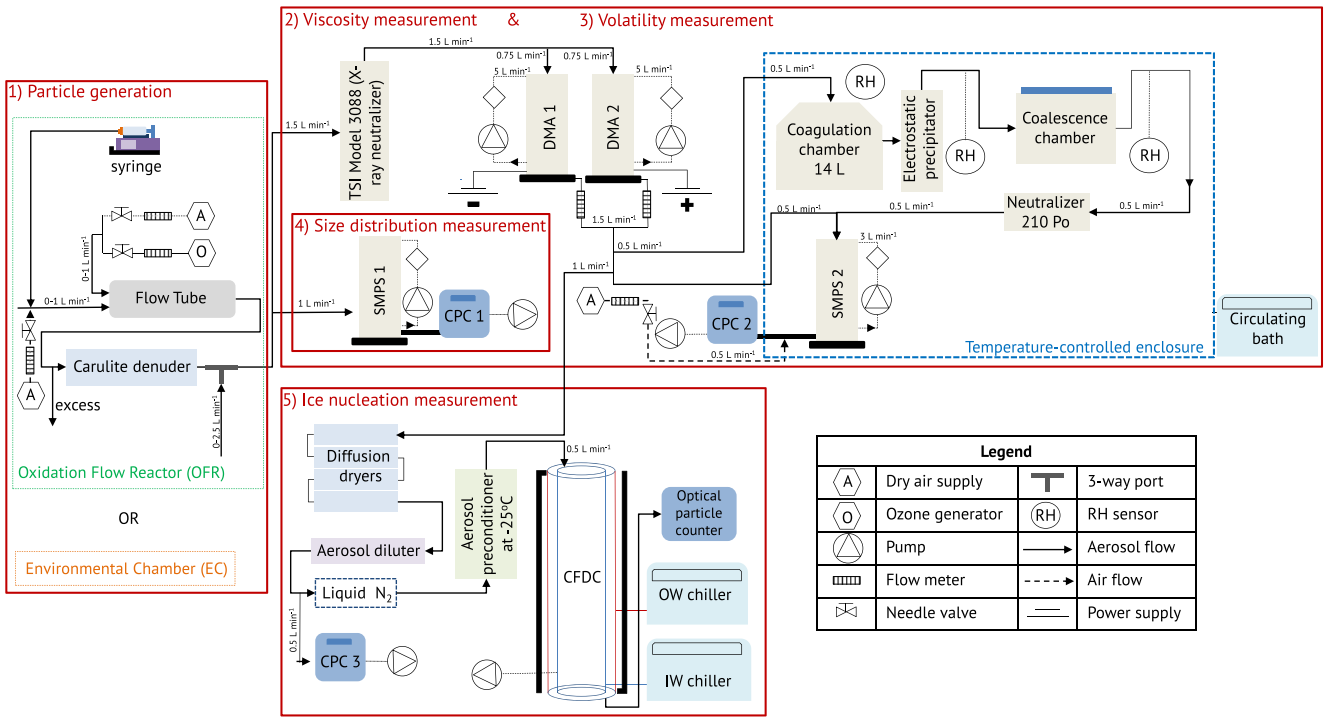


**Figure 1.** Schematic view of the experimental setup for particle generation, viscosity experiments, volatility experiments, size distributions, and IN measurements.

### 2.1. Particle Generation

The three major classes of biogenic volatile organic compounds (BVOC) are monoterpenes ($C_{10}$), sesquiterpenes ($C_{15}$), and isoprene ($C_5$) (Sakulyanontvittaya et al., 2008). These large biogenic emissions are coming from biological activity and are predominantly terrestrial and marine (Shaw et al., 2010) in origin. Models predict that ∼50%, ∼15%, and ∼3% of SOM are generated from isoprene, monoterpene, and sesquiterpenes, respectively (Guenther et al., 2012). Anthropogenic emissions contribute ∼9% (Hallquist et al., 2009). Twelve unique precursors were used to generate SOM. Precursors included monoterpenes (α-pinene (99%), β-pinene (99%), $\Delta^3$-carene (99%), limonene (97%), ocimene (>90%), sabinene (99%), terpinolene (93%)), sesquiterpene (β-caryophyllene (99%), humulene (98%)) and aromatic precursors (catechol (99%), naphthalene (98%), and resorcinol (>99%)). These precursors are important contributors to the overall monoterpene, sesquiterpene, and anthropogenic volatile organic compounds (VOC) emissions (Gu et al., 2021; Sakulyanontvittaya et al., 2008; Shilling et al., 2013). SOM was generated using either an OFR or an EC. The OFR was manufactured in-house and was the same as described in S. Petters et al. (2019). The reactor consisted of a flow tube with a sheath and central inlet flow. The central flow was injected into the center of the tube at several cm distance from the entry point. The sheath flow consisted of a mixture of hydrocarbon-free zero air and the monoterpene precursor. SOM precursor was generated by injecting liquid monoterpene/sesquiterpene into a T-fitting at a flow rate of several nL/min via a syringe pump. Air flow through the T-fitting volatilized the terpene and transported it into the flow tube via the sheath inlet. The central flow consisted of a mixture of hydrocarbon-free zero air and ozone ($O_3$) generated from a corona discharge. Diffusion of ozone into the sheath flow inside the flow tube resulted in rapid oxidation of the precursor and the formation of SOM. The net result was a continuous source of high particle number concentration with a stable size distribution. In a typical experiment, the spectral density (dN/dlnD) at the peak of the distribution is $8 \times 10^6$ cm$^{-3}$ $\pm$ $2 \times 10^6$ cm$^{-3}$ and a peak between 200 and 250 nm, and in EC is $2.9 \times 10^5$ cm$^{-3}$ $\pm$ $1.9 \times 10^5$ cm$^{-3}$ and a peak between 80 and 300 nm. Slight adjustments of the sheath and central flow rates provided moderate control over particle number concentration, mass concentration, and mode diameter of the aerosol. Typical flow total air flow through the reactor was 1.6 L min$^{-1}$, resulting in an average residence time inside the reactor of ∼65 s. Extreme ozone concentrations (∼2,000 ppm) were needed to produce sufficient aerosol at this time scale. Passing the outflow through two diffusion driers filled with Carulite catalyst removed most of the

ozone. Characterization experiments prior to this campaign showed that after the catalyst were ~0.5–3 ppm (S. Petters et al., 2019).

The continuous source of high number concentration and stable size distribution are desirable properties for experimentation. The produced particles are viscous at room temperature and the setup is ideally suited for viscosity measurement described further below. However, this OFR particle generation method of particle generation has also disadvantages. Only dark ozonolysis reaction products can be studied. The resulting high mass concentrations, typically several mg $m^{-3}$, are orders of magnitudes larger than atmospheric conditions, resulting in partitioning of more volatile compounds into the particle phase. For example, the data used in S. Petters et al. (2019) and Grayson et al. (2016) have mass loadings of 0.01–0.04 mg $m^{-3}$ and 0.121 and 14 mg $m^{-3}$, respectively. In comparison, this study used mass loadings of ~0.1–64 mg $m^{-3}$, approximately corresponding to the upper limit of the Grayson et al. (2016). They report that viscosity for α-pinene SOM varied by a factor of 45 over their range (0.01–14 mg $m^{-3}$). Using that factor of 45, we estimate that this corresponds to a difference in $T_g$ of ±4 K. Note that at low mass loadings the $T_g$ is expected to be larger than at high mass loadings as low mass loading implies high oxidation levels resulting a higher viscosity with higher $T_g$ values (Grayson et al., 2016). Chemical reaction mechanisms that lead to the formation of particles inside the OFR at high oxidant concentration and at short residence times are not necessarily representative of atmospheric pathways. Therefore particles were also generated using a traditional EC.

The environmental chamber (Finewax et al., 2018, 2019) was an 8 $m^3$ chamber with FEP Teflon walls. Before a reaction, the chamber was filled with particle-free zero air (<5 ppb of hydrocarbons and <1% relative humidity). Precursor was added to the chamber by evaporating a measured amount of the compound from a heated glass bulb into a stream of zero air. Subsequently, the oxidant was added. Either $O_3$, Cl radicals, OH radicals, or $NO_3$ radicals were used. Ozone was generated using a BMT 802N $O_3$ ozone generator, Cl radicals were generated by photolysis of $Cl_2$, OH radicals were generated in the presence of $NO_x$ by photolysis of mixture of methyl nitrite and NO or by reaction of ozone with tetramethylethylene in the absence of $NO_x$. $NO_3$ radicals were generated by thermal dissociation of $N_2O_5$. The precursor vapor reacted with the oxidant and the particle size distribution formed and evolved by nucleation, condensation, and coagulation. The SOM generated inside the EC (Mass loading ranges in environmental chambers are between 0.01 and 2.3 mg $m^{-3}$) spanned a broader range of chemical composition and included systems that formed much lower aerosol mass concentrations. However, the generated number concentration in these experiments was 1–2 orders of magnitude smaller, which was too low to measure viscosity.

## 2.2. Viscosity Measurement

### 2.2.1. Experimental Approach

Viscosity measurements were only performed for aerosol generated from the OFR. Viscosity was measured using the dimer coagulation isolation and coalescence (DCIC) technique (M. D. Petters, 2018; Rothfuss & Petters, 2016; Rothfuss et al., 2019). Therefore, particles exiting the OFR or the EC were charge neutralized using a bipolar ion source (TSI 3088, TSI Inc., Shoreview, MN). The flow was split between two DMAs (DMA, Model 3071, TSI Inc. and high flow DMA column) operated with opposite polarity power supplies. Both DMAs were operated at a 5 L $min^{-1}$: 0.75 L $min^{-1}$ sheath-to-sample flow ratio and the voltage was set to select the same mobility. The monodisperse sample flows from the two DMAs were merged and split between the continuous flow diffusion chamber (CFDC) and a 14 L coagulation chamber. The two DMAs transmitted particles carrying opposite charges. Some particles coagulated inside the coagulation chamber, forming charge-neutral dimers. Coagulation events with +1/−1 and +2/−2 particles produce neutral particles. The flow exiting the coagulation chamber was routed through an electrostatic precipitator (Kasparoglu et al., 2021, 2022) operated at 1.5 kV potential to remove all charged particles from the flow. Charge neutral particles transmitted through the electrostatic precipitator were passed through a temperature controlled volume which served as the coalescence chamber. The coalescence chamber was the same as used previously (Kasparoglu et al., 2021) and had a residence time of 120 s. The temperature inside the coalescence chamber was varied between 10 and 60°C to identify the relaxation temperature, where dimer particles coalesced from an hourglass-shaped geometry into spherical particles. Particle shape was characterized by continuously measuring the size distribution of the dimer particles exiting the coalescence chamber using a scanning mobility particle sizer (SMPS). The SMPS was operated at a sheath-to-sample flow rate of 2.3 L $min^{-1}$:0.5 L $min^{-1}$. All sheath flows were taken from a boiled-off liquid $N_2$ source to ensure effectively zero humidity in our setup. Changes in particle shape manifested as a shift in the

observed mobility diameter, which is discussed further below. This shape is then used to determine the viscosity. The hourglass-shaped, fully uncoalesced dimer corresponds to high viscosity states and the fully coalesced, spherical shape corresponds to low viscosities. Quantification of viscosity is only possible for transition states between uncoalesced and fully coalesced states. This part is explained in detail in Section 2.2.2. The coagulation chamber and the electrostatic filter, coalescence chamber, and SMPS were enclosed in a temperature controlled environment. Temperature was maintained between ~5 and 16°C using a ULT 95 (Fisher) circulating bath chiller interfaced with a heat exchanger that was placed inside the enclosure. The temperature was maintained in this range to ensure that freshly formed dimer particles were viscous enough to not coalesce into spherical shape prior to entering the coalescence chamber. RH was measured at the outlet of the coagulation chamber and the inlet and the outlet of the coalescence chamber using capacitive sensors (Rotronic HC2).

#### 2.2.2. Data Reduction

Data reduction followed the steps described in previous publications (e.g., Kasparoglu et al., 2021). The complete size distribution observed in SMPS 2 is complex and contains multiple modes (M. D. Petters, 2018; Rothfuss et al., 2019). The two most important modes include monomer sized particles and particles at +1/−1 coagulated particles. The origin of the monomer sized particles are a small fraction of singly charged particles that spontaneously discharge between the exit of DMAs 1 and 2 and the electrostatic filter. The mobility diameter of the +1/−1 coagulated particles are approximately $\sqrt[3]{2}$ larger than that of the monomer particles. The exact offset depends on the particle shape. Hourglass-shaped shaped dimer particles are ~1.04–1.08 times larger than spherical fully coalesced particles (Rothfuss et al., 2019). The mode diameters for these two modes were determined using a non-linear least squares curve fit to a size distribution function. In previous studies the mode diameter of the +1/−1 coagulated particles was plotted as a function of temperature in the coalescence chamber. The resulting graph shows an S-shaped curve with a plateau on either end of the graph. The plateaus correspond to fully coalesced and fully uncoalesced diameters, which are then used to determine the particle shape factor and in turn viscosity. This was not possible here, because the aerosol partially evaporated upon transit through the coalescence chamber. The monomer mode shrank only due to evaporation. The +1/−1 coagulated mode shrank due to evaporation and due to shape relaxation. Plotting the ratio of +1/−1 coagulated mode diameter to the monomer mode diameter resulted in a clean S-shaped curve shape that was fit to a logistic curve

$$\xi = 1 + \frac{3}{2} erfc\left(\frac{T - T_0}{\sigma\sqrt{2}}\right) \tag{1}$$

where $\xi$ is the particle geometry factor, *erfc* is the complementary error function, $\sigma$ is the spread parameter, $T$ is the temperature and $T_0$ is the midpoint of coalescence relaxation. The parameters $T_0$ and $\sigma$ are determined by the fit. An example of a temperature scan is given in Figure 2 for uncoalesced and fully coalesced dimer particles, including their ratio and S-shaped curve. The particle geometry factor is related to viscosity using the Frenkel sintering theory (Pokluda et al., 1997; Rothfuss & Petters, 2016) assuming the surface tension of 0.03 J $m^{-2}$ for SOM (S. Petters et al., 2019). Conversion from the particle geometry factor $\xi$ to viscosity η allows graphing the viscosity versus temperature over a relatively narrow range of viscosity (~$6 \times 10^6$ Pa s to $1 \times 10^8$ Pa s). The resulting temperature dependence of viscosity is fit to the Vogel–Fulcher–Tammann (VFT) relationship

$$\log_{10}(\eta) = A + \left(\frac{B}{T - T_0}\right) \tag{2}$$

where $A$, $B$, and $T_0$ are fitted parameters. $T_g$ is estimated by extrapolation of the VFT equation (Fulcher, 1925) to $\eta = 10^{12}$ Pa s. A ±10°C uncertainty for the resulting $T_g$ was determined from viscosity measurements of sucrose and citric acid and comparing the extrapolated $T_g$ from the VFT curve to literature values of $T_g$ (Marsh et al., 2018; Rothfuss & Petters, 2017a).

#### 2.2.3. Temperature and Humidity Dependent Viscosity Experiments

S. Petters et al. (2019) reported temperature and humidity dependent measurement of $\Delta^3$-carene/$O_3$ and α-pinene/$O_3$ derived SOM using the same flow reactor as described in Section 2.1. Their data shows isopleths of transition between $4 \times 10^5$ and $6 \times 10^6$ Pa s in the $T$ and RH state space. A unique result from that study was that $\Delta^3$-carene/$O_3$ derived SOM never relaxed into spheres at temperatures colder than 0°C and RH < 96%. This suggests that $\Delta^3$-carene/$O_3$ derived SOM is an excellent model system for a glassy monoterpene derived aerosol

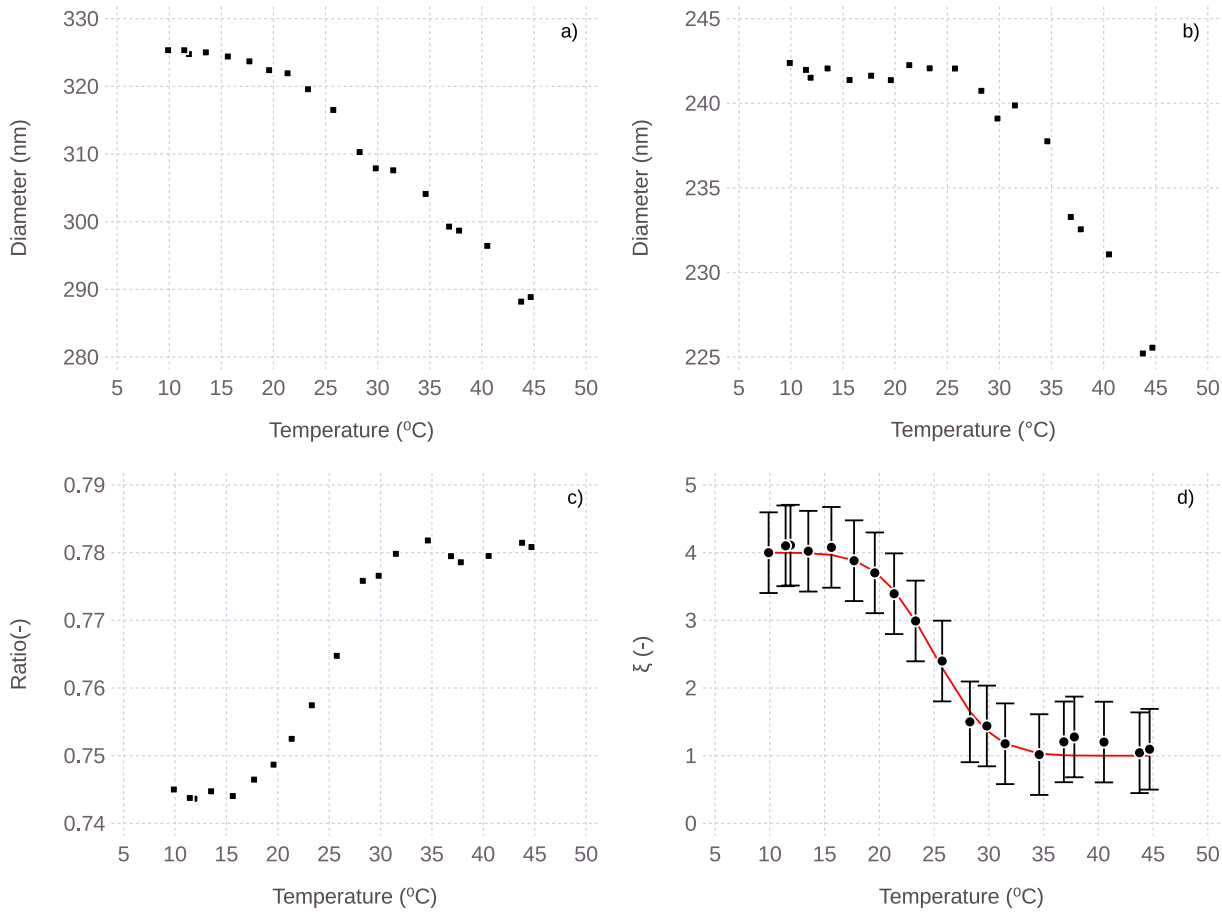


**Figure 2.** Example temperature fitting for terpinolene/$O_3$ derived secondary organic material. (a) +1/−1 coagulated mode diameter, (b) monomer diameter, (c) ratio of +1/−1 coagulated mode diameter to monomer diameter, (d) logistic curve fit to S-shaped curve. The midpoint of logistic fit is 25.1°C and $\sigma$ is 4.1°C.

under upper free-tropospheric conditions. However, an open question raised in S. Petters et al. (2019) was the short residence time of 5 s in their coalescence chamber. Thus a potential explanation for their observation is that kinetic limitations of water uptake prevented shape relaxation. If true, the longer residence time in the CFDC (17 s) might lead to water uptake, thus invalidating the assumption that the $\Delta^3$-carene/$O_3$ and other monoterpene/$O_3$ derived SOM is viscous/glassy. We, therefore, repeated the humidity-dependent experiments by increasing the coalescence relaxation from 5 to 120 s. The experimental setup and method used were the same as Kasparoglu et al. (2021). The method is similar to the viscosity measurements described above. The main difference is that humified sample flow is used. During RH scans, the temperature in the coalescence chamber is lowered, which temporarily raises the RH, which in turn induces coalescence.

### 2.3. Volatility Measurement

The volatility measurements were performed for both OFR and EC measurements, using the same procedure. In volatility tandem DMA setups mobility size-selected particles pass through an evaporation conditioner. Thermodenuders (Burtscher et al., 2001; Faulhaber et al., 2009; Huffman et al., 2008; Wehner et al., 2002) are often used to accelerate evaporation. The size distribution is measured after the thermodenuder to determine the mass or volume fraction remaining (Bilde et al., 2015; Champion et al., 2019; Mendes et al., 2016; Oxford et al., 2020). Here we infer volatility from the shrinkage of monomer mode diameter upon passage through the coalescence chamber. Figure 3 shows an example. The temperature scan ranges from 20 to 60°C. Particle evaporation depends on the temperature, residence time, the particle diameter, and chemical composition (Rader et al., 1987; Wright et al., 2016). Since the scanned temperature range was not the same for all of the experiments we restrict the measurement to a narrower range. Specifically, we define volatility operationally by the volume fraction remaining

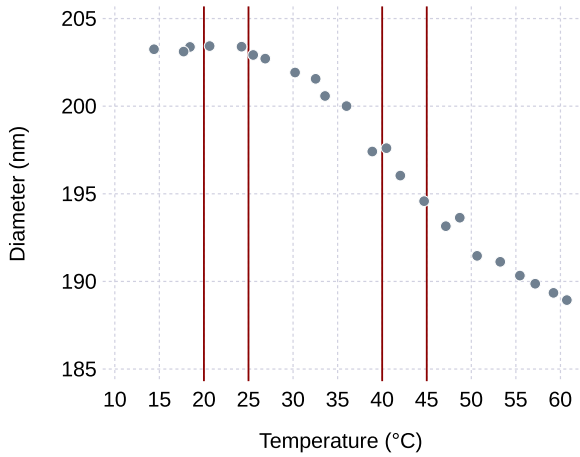


**Figure 3.** Evolution of the monomer mode diameter during a temperature scan for β-caryophyllene/$O_3$ derived secondary organic material (E1). The red vertical lines show the warm and cold temperature ranges used to derive volume fraction remaining.

(VFR), which is calculated as the ratio of the mean sphere-equivalent particle volume derived from the mode diameters falling inside the temperature ranges 40°C < $T$ < 45°C and 20°C < $T$ < 25°C. Note that although residence time was constant for all experiments, the monomer diameter was not. This was because the monomer size was tied to the optimal size for the dimer generation experiment. However, some of the EC experiments produced insufficient number concentration at these larger sizes, and thus the size needed to be adjusted. Since evaporation rate depends on size, the VFRs are only directly comparable when considering the same monomer diameter.

### 2.4. Size Distribution Measurement

The size distributions from the OFR and EC were measured using the self-contained SMPS 1 in Figure 1. The SMPS consisted of a TSI 3081 column operated at a 9 L $min^{-1}$:1 L $min^{-1}$ sheath-to-sample flow ratio and using a TSI 3771 CPC as detector. The instrument scanned from 10 kV to 10V over 2 min. The raw data were collected into 120 size bins from 30 to 300 nm and inverted as described in M. D. Petters (2018). The volume concentration of an experiment for each scan was calculated by integrating over the size distribution and assuming that particles are spheres. Although the mode diameters of the size distribution were less than 300 nm, some unknown fraction of particles exceeded the upper diameter limit of the DMA. Therefore the reported volume concentrations are a low biased approximation of the true volume concentration.

### 2.5. Ice Nucleation Measurements Within the Onset Conditions Through a CFDC

#### 2.5.1. Experimental Setup

Ice nucleating particle concentrations were measured using the Colorado State University low temperature CFDC (Patnaude et al., 2021) based on previous designs (DeMott et al., 2009). The instrument consists of an annular section of two cylinders with iced walls held at two different temperatures. The outer wall was warmer than the inner wall, which created a supersaturation with respect to ice in the center of the annulus. Aerosols passed to the CFDC (see Figure 1) were further dried by diffusion dryers and a cold trap. Particles were passed through a cold trap that was immersed in the bath volume of the chiller providing cooling to the CFDC inner wall, then subsequently through a short section of tubing immersed in liquid nitrogen. The cold trap through the chiller bath was approximately 5 m of coiled ¼ inch copper tubing, while the section in liquid nitrogen was ∼20 cm of the same tubing in a U shape. This ensured that the aerosol sample flow frost-point temperature was <−70°C. Subsequently the sample was warmed again to room temperature. This ensures that the starting RH is close to zero and that RH never exceeds the value at the IN measurement conditions. The particle number concentration was reduced by splitting the flow, passing a fraction of the sample through a filter, followed by remerging the flow. A needle valve controlled the split between the filter and the bypass. The needle valve was adjusted to achieve concentrations <10,000 $cm^{-3}$ entering the CFDC to prevent saturation of the detectors. Particle concentration entering the CFDC was monitored using CPC 3 (TSI 3010) operated at 0.5 L $min^{-1}$ flow rate. The remaining flow entered a thermal preconditioner, which cooled the sample to −25°C prior to entering the CFDC inlet. The purpose of the preconditioner is to accelerate equilibration of the sample after it enters the main section of the instrument. The thermodynamics trajectory of the particles is complex. We assert that the RH of the sample is low. It is possible that the particles are not glassy at room temperature and it is likely that the viscosity varies along that trajectory. The dilution might result in some repartitioning of the SOM via evaporation, which would raise the viscosity of the particles based on the data by Grayson et al. (2016). In any case, we expect that the particles turn glassy again inside the precooler, based on the results shown in Figure 4, Table 1, and data in S. Petters et al. (2019). The CFDC was operated at a sheath-to-sample flow ratio of 4.5 L $min^{-1}$:0.5 L $min^{-1}$. The temperature and RH with respect to ice at the aerosol lamina depend on the inner and outer wall temperature. The $RH_{ice}$ was computed from the wall temperatures and using the vapor pressure parameterization of Murphy and Koop (2005). Note that there are several different sources of measurement uncertainty within the CFDC measurements. The first is that the conditions (temperature and SSice) an aerosol experiences varies depending on its position within the aerosol

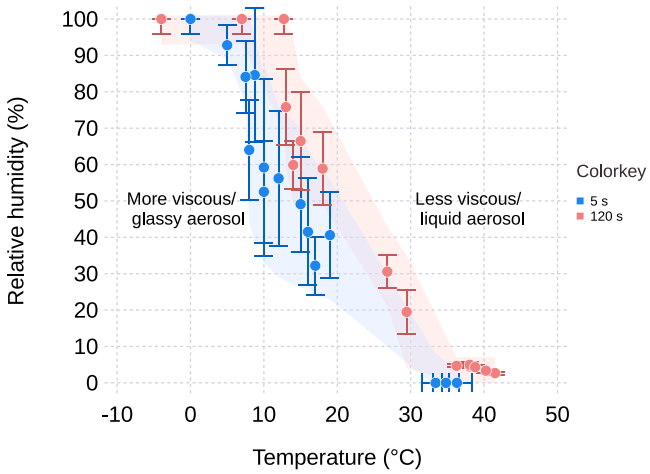


**Figure 4.** Viscous phase transition as a function of $T$ and RH for $\Delta^3$-carene/$O_3$ derived SOM for residence times of 5 s (S. Petters et al., 2019) and 120 s (this study). Circles correspond to the midpoint of one $T$ or RH scan. Points near 0% RH show $T$-scans. Horizontal bars ($T$ scans) and vertical bars (RH-scans) show the viscosity transition defined by the standard deviation of the logistic curve (Equation 1). The viscosity corresponds to $4 \times 10^5$ to $6 \times 10^6$ Pa s for 5 s residence time and $1.4 \times 10^7$ to $2.8 \times 10^8$ Pa s for 120 s residence time. Temperatures lower than the shaded areas circumscribe the transition regime. Thermodynamic states colder than the shaded areas correspond to more viscous and glassy states.

lamina and uncertainties in the measurements (temperatures, pressure, flows) that feed into the aerosol lamina calculations. Attempts have been made to characterize this uncertainty in several publications for similar instruments (DeMott et al., 2015; Richardson, 2009) constraining the absolute uncertainty to less than 5.5% ice supersaturation and −40°C to less than 9% at −60°C. Data collected with this instrument (Patnaude et al., 2021) agree very well with measurements of similar systems (Ladino et al., 2016; Schill & Tolbert, 2014; Wagner et al., 2017). During a typical experiment, the instrument was set to $RH_{ice}$ near 100% and the wall temperatures were set to diverge to increase $RH_{ice}$ while approximately holding the aerosol lamina temperature constant. Note that the approximate rate is ∼1.5% $RH_{ice}$/min and calculated based on first scans of a few experiments (E3, E4, E14, and E18). Ice crystal number concentration was measured using an optical particle counter (CLiMET, model CI-3100). Raw signals for all particles were collected using an NI USB-DAQ 6366 operating at 2 megasamples/s. The peak voltage for each particle detection was recorded. Particles with peak voltages exceeding those of 2.5 μm polystyrene latex spheres were considered frozen. Particles with smaller peak voltages were considered as not activated. The lower size cut of the optical particle spectrometer was ∼0.3 μm. Ice active fractions are derived from the ratio of INP and the number concentration measured by the CPC that is entering the CFDC. The onset conditions for IN were defined as the temperature/saturation ratio when the ice fraction increased by one order of magnitude relative to the background. Typical backgrounds were 0.05%, and thus typical onset conditions corresponded to 0.5% activated fraction.

### 2.6. Verification of CFDC Functionality

Figure 5 shows the observed frozen fraction curves for citric acid particles at −62°C. The bluedata points show a heterogeneous freezing onset at 130% $RH_{ice}$ which is similar to the heterogeneous onset for citric acid observed by Murray et al. (2010). The red data show the homogenous freezing onset at 165% $RH_{ice}$, which is consistent with the prediction of Koop et al. (2000) for liquid haze particles. The difference between the two experiments is the degree to which the particles are dried before entering the precooler and CFDC. More drying, by including the cold trap, leads to the formation of glassy citric acid which freezes heterogeneously, while less drying leads to the formation of semi-solid or liquid citric acid which freezes homogeneously. The maximum observed activated fraction differs between homogeneous and heterogeneous freezing, which we believe to be due to the different nucleation rates between the two mechanisms. Generating glassy citric acid through diffusion and cold trap drying in our setup is extremely challenging due to the combination of a glass transition temperature of ∼10°C and 0% RH at room temperature, the high hygroscopicity of citric acid, and uncertain kinetics of water loss from wet citric acid particles. To achieve glassy conditions the sample RH must be below 10% at 5°C (Kasparoglu et al., 2021), which corresponds to a sample frost-point temperature of −24°C. We did not have a direct measurement of the lowest RH achieved during drying of the atomized particle flow. Additionally, we cannot be certain that the aerosol has reached equilibrium water content, which may require timescales in excess of several minutes, with measurements becoming increasingly uncertain at lower temperature and RH (Davies & Wilson, 2016; Ingram et al., 2017). However, the observations here indicate that with our maximum drying capacity, glassy citric acid was produced. Furthermore, the observations demonstrate that the CFDC correctly measured heterogeneous freezing of glassy aerosol when such aerosol was present. Note that all SOM was generated in dry zero air ($T_{frost} < -40$°C, the readings for dew point less than 0°C is defined as $T_{frost}$) and that the sample was further dried by the $N_2$ sheath flow in the DMAs. Thus drying the particles to effectively zero RH prior to entering the CFDC is much less of an issue than with the citric acid experiments.

#### 2.6.1. Literature Data

Data was digitized from prior studies to compare to our measurements. Data for α-pinene/$O_3$ was digitized from Figure 4 in Koehler et al. (2010), Figure 3 in Ladino et al. (2014), Figure 5 in Ignatius et al. (2016), Figure 5a

**Table 1**
*Summary of Experimental Data*

| Precursor-OFR/$O_3$ | Code | $T_r$ (°C) | $T_g$ (°C) | VFR | 20°C < $D_{mono}$ (nm) < 25°C | Volume (μm$^3$ cm$^{-3}$) | Onset | Onset $T$ (°C) | Onset $RH_{ice}$ (%) | CPC (# cm$^{-3}$) |
|---|---|---|---|---|---|---|---|---|---|---|
| β-caryophyllene | E10 | 39.9 ± 4.3 | 23.2 ± 3.6 | 0.85 | 205 | 11,985 ± 1,756 | No | −64.9 | 187 | 3,177 |
| Limonene | E8 | 37.8 ± 5.5 | 16.6 ± 2.6 | 0.94 | 245 | 45,857 ± 12,763 | No | −67.8 | 165 | 3,420 |
| Sabinene | E16 | 30.4 ± 3.6 | 16.3 ± 7.1 | 0.92 | 247 | 47,499 ± 5,381 | No | −60.8 | 218 | 3,078 |
| α-pinene -high conc. | E3 | 37.6 ± 6.8 | 15.8 ± 1.7 | 0.86 | 248 | 60,831 ± 30,517 | Yes | −57 | 182.5 | 3,968 |
| Sabinene | E19 | 26.3 ± 4.1 | 8.5 ± 0.3 | 0.83 | 144 | 35,609 ± 1,061 | | | NA | |
| Terpinolene | E6 | 23.1 ± 4.1 | 8.1 ± 5.0 | 0.82 | 245 | 63,797 ± 15,110 | No | −56.8 | 180 | 4,048 |
| $\Delta^3$-carene | E2 | 27.3 ± 5.0 | 7.27 ± 8.9 | 0.90 | 245 | 60,414 ± 20,796 | No | −48 | 155 | 3,923 |
| Humulene | E12 | 35.1 ± 7.0 | 5.7 ± 8.0 | 0.89 | 200 | NA | No | −53.6 | 220 | 3,209 |
| Humulene | E14 | 31.0 ± 6.5 | 5.8 ± 5.5 | 0.90 | 194 | 11,215 ± 10,155 | No | −58.5 | 180 | 2,796 |
| Ocimene | E7 | 27.1 ± 5.5 | 5.7 ± 2.3 | 0.91 | 243 | 21,582 ± 24,738 | No | −59.3 | 180 | 4,026 |
| Precursor-EC | Code | $T_r$ (°C) | $T_g$ (°C) | Volatility (−) | $D_{mono}$ (nm) | Volume (μm$^3$ cm$^{-3}$) | Onset | Onset $T$ (°C) | Onset $RH_{ice}$ (%) | CPC (# cm$^{-3}$) |
| β-caryophyllene/$O_3$ | E1 | NA | | 0.84 | 202 | 2,171 ± 1,184 | No | −65.75 | 196 | NA |
| | | | | | | | No | −61.5 | 189 | |
| β-caryophyllene/$O_3$ | E4 | | | 0.91 | 231 | 7,048 ± 6,159 | Yes | −59 | 185 | 196 |
| Catechol/Cl | E5 | | | 0.90 | 240 | 1,441 ± 229 | Yes | −58.8 | 165 | 2,100 |
| | | | | | | | | −54.4 | 158 | |
| Resorcinol/OH | E9 | | | 0.87 | 223 | 3,993 ± 6,402 | Yes | −70.2 | 208 | 670 |
| Naphthalene/OH | E11 | | | 0.93 | 248 | 2,537 ± 608 | Yes | −65 | 211 | 1,644 |
| β-pinene/$NO_3$ | E13 | | | na | na | na | No | −69.6 | 208 | 400 |
| Catechol/OH | E15 | | | 0.90 | 251 | 2,287 ± 806 | Yes | −64.5 | 185 | 77 |
| | | | | | | | | −60.4 | 174 | |
| | | | | | | | | −56 | 165 | |
| | | | | | | | | −51.7 | 158 | |
| $\Delta^3$-carene/$O_3$ | E17 | | | 0.83 | 151 | 49 ± 2 | No | −61.3 | 174 | 238 |
| | | | | | | | Yes | −61 | 184 | |
| | | | | | | | Yes | −60.8 | 194 | |
| α-pinene/$O_3$ -low conc | E18 | | | 0.96 | 86 | 11 ± 3 | Yes | −62.6 | 171 | 538 |
| | | | | | | | | −62.5 | 177 | |
| | | | | | | | | −55.6 | 164 | |
| | | | | | | | | −50 | 154 | |
| | | | | | | | | −46.3 | 152 | |

*Note.* Columns from left to right correspond to, precursor generation, experiment code to relate to raw data, observed relaxation temperature from the logistic curve in Equation 1, estimated glass transition temperature, volatility (volume fraction remaining, VFR) derived from monomer shrinkage, monomer diameter, aerosol volume concentration derived from SMPS data, whether IN onset for homogeneous or heterogeneous freezing (see text for definition) was observed, temperature at onset, relative humidity with respect to onset, and total particle concentration sampled by the CFDC. If no onset was observed, onset $T$ and onset $RH_{ice}$ correspond to the conditions at largest $RH_{ice}$ probed. NA in $T_r$ and $T_g$ columns for EC experiments indicate that there is no measurement. Other NA indicates that there is no clear data for the cells.

in Möhler et al. (2008), Figure 2 in Piedehierro et al. (2021), and Figure 3a in Wagner et al. (2017). Data for limonene and isoprene derived SOM was digitized from Figure 3a in Wagner et al. (2017) and Figure 4 in Wang et al. (2012), respectively. Data for naphthalene/OH was digitized from Figure 2 in Wang et al. (2012).

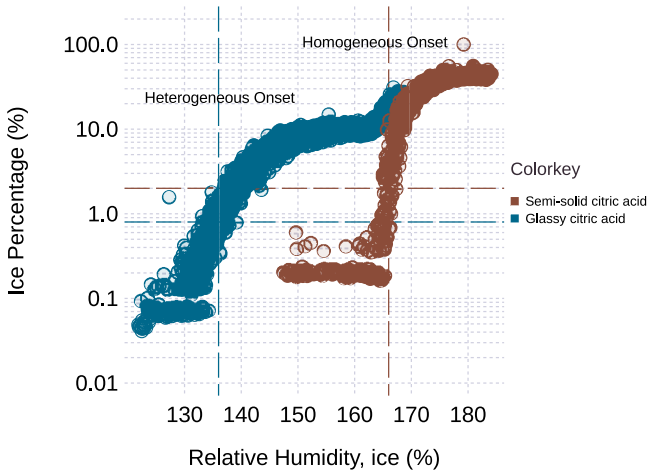


**Figure 5.** Observed activated percentage curves for 300 nm citric acid particles at −62°C. Each point corresponds to 1 Hz data. The horizontal lines indicate an increase of 1 order of magnitude above the background concentration.

## 3. Results

### 3.1. RH-Dependent Viscosity Data

Figure 4 shows the viscous phase transition as a function of $T$ and RH for $\Delta^3$-carene/$O_3$ for residence times of 5 and 120 s. The longer residence time data show a similarly steep isopleth compared to the 5 s data. However, the 120 s residence time data appear to be slightly shifted to warmer conditions. This is consistent with the fact that the 120 s residence time data correspond to more viscous states. More viscous states require a higher temperature or RH to relax into a sphere. The main observation is that the relaxation into a sphere is not observed for either residence time at any RH at lower temperatures. Based on observed VFT slopes of temperature versus viscosity, particles turn glassy at ∼20–30°C below the relaxation temperature (Marsh et al., 2018; Rothfuss & Petters, 2017b; S. Petters et al., 2019). Table 2 summarizes the VFT fits from this study. Here the difference between $T_r$ and $T_g$ are on the same order of magnitude. We further note that SOM generated in our OFR from different monoterpene precursors have similar temperature and humidity dependence to the results shown here. Thus, we conclude that SOM from $\Delta^3$-carene/$O_3$, and probably all SOM from monoterpene precursors generated in our OFR, is glassy at all conditions encountered in the CFDC. At conditions exceeding the critical supersaturation, the particle is expected to activate as CCN followed by homogeneous freezing of water. For dissolved particles the critical supersaturation is <1% ($RH_{water}$ < 101%). For insoluble, but wettable particles the critical supersaturation is given by the Kelvin equation (e.g., Petters & Kreidenweis, 2007). For insoluble particles that are hydrophobic and have a contact angle >0, the critical supersaturation may exceed $RH_{water}$ 200% and the value depends on the contact angle (Mahata & Alofs, 1975).

### 3.2. Volatility Data

Results are reported in Table 1, which shows volatility in terms of VFR in the range 40°C < $T$ < 45°C, 60 s residence time, and the associated dry diameter prior to passage through the heated section. The observed VFRs are between 0.82 and 0.94 for the OFR experiments and between 0.83 and 0.96 for the EC experiments. Saha and Grieshop (2016) quantified VFR for α-pinene ozonolysis products with a dual thermodenuder between 0 and 120°C. In their experiments the VFR was 0.7 and 0.9 at 40°C and at 50 s residence time for high and low mass loadings, respectively. Their data shows that the VFR decreases with increasing mass loading. Kolesar et al. (2015) also studied the mass loading effect on volatility. In contrast to Saha and Grieshop (2016), they showed that there is no significant dependency of VFR on mass loading. In Kolesar et al. (2015), the VFR for α-pinene ozonolysis products was between 0.8 and 0.9 at ∼46°C and at 26 s residence time for low (0.001–0.03 mg $m^{-3}$) and high mass loading (0.4–0.8 mg $m^{-3}$) cases, respectively. They also implied that the $T_{50,}$ which is the temperature at which the VFR becomes 0.5, was independent of the mass loading. The range of mass loadings in these studies was 0.005–0.445 mg $m^{-3}$ (Saha & Grieshop, 2016), 0.001–0.8 mg $m^{-3}$ (Kolesar et al., 2015), and $T_{50}$ independency for the ranges 0.4–0.8 mg $m^{-3}$ (Kolesar et al., 2015). This contrasts to the range of mass loadings used here, which ranged from 0.011 to ∼64 mg $m^{-3}$ assuming unit density based on volume concentrations in Table 1. Partitioning theory suggests that VFR increases with decreasing mass loading for the same aerosol composition (Donahue et al., 2009; Odum et al., 1996; Pankow, 1994). The data in Table 1 imply no systematic relationship between the volume concentration and the VFR. We attribute this to several reasons. First, particles from the flow-tube are sampled immediately after formation and the aerosol likely did not have enough time to fully equilibrate with the gas phase. Second, the data include multiple precursors, and thus cover a wide range of chemical compositions. Third, the sizes were not equal in all experiments, thus making it difficult to directly compare the VFRs between those data. Inversion to infer intensive properties such as vapor pressure or saturation concentration were not attempted from this limited data set. Finally, the volume concentrations are highly approximate as particles >300 nm were not measured by the SMPS, thus missing an unknown fraction of the total volume concentration. Nevertheless, our data highlight two important points. First, the VFRs reported here are consistent with previous observations at similar residence times and temperatures (Kolesar et al., 2015; Saha &

**Table 2**
*Vogel–Fulcher–Tammann Fit Parameters A, B, and $T_0$, Midpoint of Fit Parameters, σ Values and $T_g$ for Oxidation Flow Reactor Experiments*

| Precursor | Code | $T_r \pm \sigma$ (°C) | $T_g$ (°C) | A | B | $T_0$ |
|---|---|---|---|---|---|---|
| Δ3-carene | E2 scan1 | 25.7 ± 7.6 | −5.0 | 2.969 | 234.253 | 242.207 |
| Δ3-carene | E2 scan2 | 27.5 ± 6.3 | 2.3 | 3.281 | 172.077 | 255.742 |
| Δ3-carene | E2 scan3 | 28.1 ± 3.0 | 16.7 | 3.605 | 69.130 | 281.593 |
| Δ3-carene | E2 scan4 | 25.8 ± 2.3 | 15.7 | 1.734 | 114.439 | 277.706 |
| Δ3-carene | E2 scan5 | 29.8 ± 8.1 | −2.5 | 3.166 | 229.829 | 244.650 |
| Δ3-carene | E2 scan6 | 26.4 ± 3.7 | 12.3 | 2.826 | 113.509 | 273.107 |
| Δ3-carene | E2 scan7 | 27.4 ± 4.4 | 11.3 | 3.948 | 83.638 | 274.088 |
| α-pinene | E3 scan1 | 40.5 ± 6.4 | 17.0 | 3.927 | 123.518 | 274.853 |
| α-pinene | E3 scan2 | 34.7 ± 5.4 | 14.6 | 3.812 | 110.974 | 274.216 |
| β-caryophyllene | E10 scan1 | 39.8 ± 3.3 | 27.282 | 3.503 | 78.754 | 291.163 |
| β-caryophyllene | E10 scan2 | 40.3 ± 5.0 | 20.554 | 3.246 | 136.609 | 278.098 |
| β-caryophyllene | E10 scan3 | 39.5 ± 4.6 | 21.777 | 3.574 | 108.113 | 282.096 |
| Limonene | E8 scan1 | 38.7 ± 5.1 | 18.398 | 3.310 | 137.565 | 275.717 |
| Limonene | E8 scan2 | 37.0 ± 5.9 | 14.776 | 3.780 | 124.271 | 272.807 |
| Humulene | E12 scan1 | 34.9 ± 4.7 | 17.491 | 3.821 | 100.423 | 278.364 |
| Humulene | E12 scan2 | 36.0 ± 8.4 | 3.214 | 3.421 | 221.907 | 250.498 |
| Humulene | E12 scan3 | 34.3 ± 7.8 | 4.051 | 3.426 | 204.771 | 253.318 |
| Ocimene | E7 scan1 | 29.2 ± 6.4 | 4.047 | 3.396 | 164.468 | 258.083 |
| Ocimene | E7 scan2 | 24.9 ± 4.6 | 7.319 | 3.639 | 104.696 | 267.947 |
| Humulene | E14 scan1 | 35.7 ± 9.5 | −0.023 | 3.681 | 208.813 | 248.025 |
| Humulene | E14 scan2 | 30.1 ± 6.1 | 7.695 | 3.841 | 122.230 | 265.864 |
| Humulene | E14 scan3 | 26.9 ± 5.6 | 3.023 | 2.361 | 223.513 | 252.985 |
| Humulene | E14 scan4 | 31.2 ± 4.9 | 12.432 | 3.601 | 113.234 | 272.100 |
| Sabinene | E19 scan1 | 27.2 ± 4.2 | 8.716 | 2.219 | 198.600 | 261.560 |
| Sabinene | E19 scan2 | 25.4 ± 4.2 | 8.303 | 3.138 | 136.058 | 266.101 |
| Sabinene | E16 scan1 | 32.2 ± 2.9 | 21.268 | 3.785 | 60.798 | 287.017 |
| Sabinene | E16 scan2 | 28.6 ± 4.4 | 11.276 | 3.311 | 117.296 | 270.927 |
| Terpinolene | E6 scan1 | 23.5 ± 5.9 | 0.960 | 3.590 | 136.832 | 257.840 |
| Terpinolene | E6 scan2 | 23.3 ± 3.8 | 8.647 | 3.460 | 93.555 | 270.842 |
| Terpinolene | E6 scan3 | 20.8 ± 2.6 | 12.729 | 5.043 | 24.303 | 282.385 |
| Terpinolene | E6 scan4 | 25.0 ± 4.1 | 9.919 | 3.929 | 79.456 | 273.224 |

Grieshop, 2016). Second, the range of VFRs in the EC and OFR experiments was 0.89 ± 0.04 and 0.88 ± 0.04, respectively. The ranges for the EC experiments are similar and on average slightly larger than those in the OFR experiments. Since VFR and viscosity correlate (Champion et al., 2019; Li et al., 2020), we expect that the particles generated in the EC were at least as viscous as those generated in the OFR. However, we do not have direct measurements to confirm this conjecture.

### 3.3. Ice Nucleation Data for SOM

#### 3.3.1. α-Pinene/$O_3$

Figure 6 shows ice formation conditions on α-pinene/$O_3$ SOM. The freezing onset observed in this study (squares and diamonds) is above the homogeneous freezing line and in 15 out of 34 experiments above water saturation. Note that the water saturation line is calculated and depends on the assumed vapor pressure parameterization.

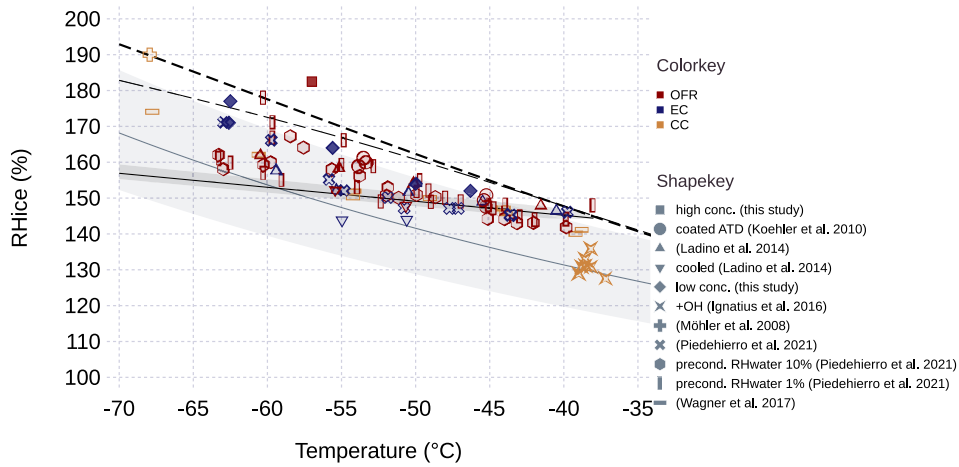


**Figure 6.** Relative humidity with respect to ice required for the ice formation onset of pure organic or organic coated particles generated from α-pinene/$O_3$ oxidation. Color encodes the generation method. Shapes encode the data source when onset was observed according to the onset criterion. Filled symbols represent data from this study, corresponding to an increase of one order of magnitude above background conditions (~0.5% ice active fraction). Onset conditions for IN of the literature data are as follows: 1% of particles are activated for SOM coated Arizona test dust (ATD) in Koehler et al. (2010); 0.1% of particles in Ladino et al. (2014); frozen particles represent 10% in Ignatius et al. (2016); 1% of particles in Möhler et al. (2008); 0.1% of activated fraction in Wagner et al. (2017); and 1% of activated fraction in Piedehierro et al. (2021). The dashed black line corresponds to water saturation (Buck, 1981; Buck Research Instruments, LLC, 2010). The long-short-long black line corresponds to water saturation computed by Murphy and Koop (2005). The black solid line corresponds to the homogeneous freezing of solution droplets according to Koop et al. (2000). The shaded area corresponds to the homogeneous freezing range denoting from 50 to 5,000 nm. The gray line and light gray shaded area correspond to the homogeneous freezing line of aqueous sulfuric acid aerosol particles proposed by Schneider et al. (2021).

Figure 6 illustrates this uncertainty by superimposing water saturation lines computed using the parameterizations of Murphy and Koop (2005) and Buck (1981). The onset for α-pinene/$O_3$ aerosol generated by the OFR (filled red square) is above the water saturation limit. To rule out potential instrument malfunction, we tested the system against room air and observed homogeneous freezing near the expected Koop et al. (2000) conditions. Requiring conditions far in excess of water saturation to activate cloud droplets on particles, followed by freezing of the pure water, suggest that the material has a contact angle >0 (Mahata & Alofs, 1975), henceforth referred to as hydrophobic. Note that this relationship between contact angle, critical supersaturation, and onset conditions only applies to data points that exceed water saturation in this study. The relationship between critical supersaturation and contact angle is given in their Figure 3. The point above water saturation (red filled square) is at $RH_{water}$ = 105.5%, which implies a contact angle >20°. In contrast, α-pinene/$O_3$ samples generated in the EC (blue diamonds) froze between the limits of homogeneous freezing nucleation and water saturation. This suggests that these particles take up some water hygroscopically and subsequently freeze. The results from the α-pinene/$O_3$ SOM generated in the EC are broadly consistent with the data reported by Koehler et al. (2010), Ladino et al. (2014), and Möhler et al. (2008). In contrast, the precooled experiments from Ladino et al. (2014), and the experiments by Ignatius et al. (2016) resulted in heterogeneous IN of SOM particles. Neither OFR nor EC generated α-pinene/$O_3$ particles from this study nucleate ice below conditions required for homogeneous freezing of solution droplets.

### 3.3.2. Terpene Precursors

Figure 7 summarizes the IN onset for SOM generated from all the terpene precursors in the OFR with $O_3$. None of the data showed freezing conditions at or below the Koop et al. (2000) threshold for homogeneous IN. In 13 out of 20 RH-scans we found IN onset above the water saturation line. In some of the experiments no ice formation was observed, and these points are marked as filled marker symbols. One possible explanation for the high $RH_{ice}$ values reported in Figure 7 is vapor depletion in the aerosol lamina. Particle number concentration entering the CFDC was capped at ~5,000 $cm^{-3}$ through a dilution system. This number is at the low end of the concentration shown in Figure S1 of Levin et al. (2016), which summarized the reduction in apparent IN efficiency as a function of particle number concentration inside the instrument. More importantly, the vapor limitations play a role only if the particles activate as CCN. In our experiments, this did not happen due to subsaturated

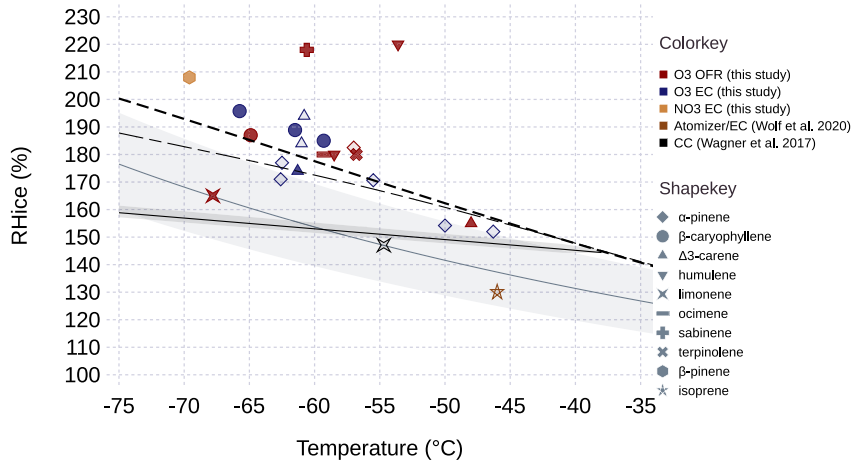


**Figure 7.** Relative humidity with respect to ice required for the ice formation onset of organic aerosol generated from oxidation of terpene precursors. Colors correspond to the generation method. Shapes denote the precursor. The open symbols represent cases when onset was observed according to the onset criterion, corresponding to an increase of one order of magnitude above background conditions (~0.5% ice active fraction). Filled symbols correspond to the maximum relative humidity probed, but no ice formation was observed. The dashed black lines correspond to water saturation as in Figure 6. The onset condition is ~0.002% in Wolf et al. (2020) and 0.1% of activated fraction in Wagner et al. (2017). The black solid line corresponds to the homogeneous freezing of solution droplets according to Koop et al. (2000). The shaded area corresponds to the homogeneous freezing range denoting from 50 to 5,000 nm. The gray line and light gray shaded area correspond to the homogeneous freezing line of aqueous sulfuric acid aerosol particles proposed by Schneider et al. (2021).

conditions with respect to liquid water. The aerosol water uptake is negligible. Therefore, vapor limitations are very unlikely to explain these observations. Again, we tested the instrument against room air at the end of each scan to verify freezing could be detected. Ice formation was observed in each case. Ice formation disappeared when switching back to the SOM source. This is consistent with the hypothesis that the SOM is hydrophobic. This is also consistent with the observation in Figure 4, and those of S. Petters et al. (2019), who found that for OFR generated α-pinene/$O_3$ and $\Delta^3$-carene/$O_3$ aerosol humidification below 0°C does not result in water uptake followed by particle dimer relaxation. Note that this is an empirical constraint obtained at coalescence residence times of 60 s which exceeds the residence time of 17 s in the CFDC. Whether the lack of liquefaction is due to kinetic limitations or solubility limitations remains unclear. Further discussion about the relationship between kinetic limitations, temperature, and water activity in relationship to the dimer relaxation measurements is given in prior work (Kasparoglu et al., 2021; S. Petters et al., 2019).

### 3.3.3. Aromatic Precursors

Figure 8 summarizes the IN onset temperatures for the aromatic precursors, namely catechol/OH/Cl, resorcinol/OH, and naphthalene/OH. Results from this study show onset temperature close to or above water saturation for all three precursors. This is in contrast to the results from Wang et al. (2012), who generated naphthalene-derived SOM using a potential aerosol mass (PAM) oxidation flow reactor. Their data show heterogeneous nucleation just below the homogeneous freezing threshold according to Koop et al. (2000).

## 4. Discussion

Our results show that a glassy or viscous phase state may be a necessary but not a sufficient condition to predict whether organic particles nucleate ice. This work adds to a growing body of literature on the IN of viscous secondary organic material at $T < -40$°C at cirrus conditions. Unique to this study is the inclusion of direct measurement of viscosity for some of the tested aerosols. None of the aerosols tested exhibited heterogeneous IN activity below homogeneous freezing conditions for solution droplets. The literature data included in Figures 6–8 show an emerging consensus across studies that complex SOM is generally not IN active below homogeneous freezing conditions for solution droplets. Note that the criteria to determine ice nucleation onset slightly differ between investigators, which makes it difficult to directly compare between studies. Generally the ice activation curves are steep functions of activated fraction versus $RH_{ice}$, which reduces the uncertainty in $RH_{ice}$ space

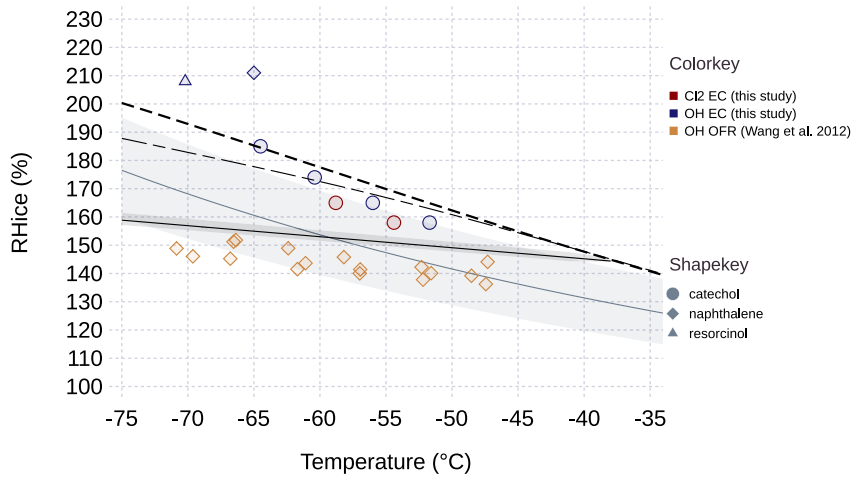


**Figure 8.** Relative humidity with respect to ice for the ice formation onset of organic aerosol generated from oxidation of aromatic precursors. Colors denote the generation method. The dashed black solid line represents the water saturation line. The onset IN conditions are determined by the optical microscope, for particle sizes larger than 0.2 μm in Wang et al. (2012). The dashed black lines correspond to water saturation as in Figure 6. The black solid line corresponds to the homogeneous freezing of solution droplets according to Koop et al. (2000). The shaded area corresponds to the homogeneous freezing range denoting from 50 to 5,000 nm. The gray line and light gray shaded area correspond to the homogeneous freezing line of aqueous sulfuric acid aerosol particles proposed by Schneider et al. (2021).

for a given discrepancy in activated fraction. Even still, using the data in Figure 6 as an example, a difference between a 0.1% and 1% activated fraction as the onset point produces a difference in $RH_{ice}$ of less than 5%. This uncertainty does not change the larger point that most systems require conditions in excess of the homogeneous IN threshold for haze particles. Exceptions are the study of Wolf et al. (2020) who show that isoprene-derived SOM particles could freeze heterogeneously, albeit at extremely low active fractions (see Figure 7). The other data that hint at heterogeneous IN activity are α-pinene derived particles by Ignatius et al. (2016) (see Figure 6) and naphthalene derived SOM in Wang et al. (2012) (see Figure 8). However, the IN onsets reported in these studies still cluster close to the homogeneous freezing nucleation threshold. As shown by the superimposed parameterization of Schneider et al. (2021) the homogeneous onset condition of Koop may be more uncertain than previously thought. Whether the ice formation in the studies of Ignatius et al. (2016) and Wang et al. (2012) resulted from homogeneous or heterogeneous ice formation,it cannot compete the much higher IN activity that is usually observed in mineral dust particles (Ansmann et al., 2019; Archuleta et al., 2005; Hoose & Möhler, 2012; Welti et al., 2009).

The viscosity measurements suggest that the terpene-derived SOM generated in the OFR is glassy and hydrophobic (see Figure 4 and S. Petters et al. [2019]). Note that even SOM generated from the same precursor will have slight differences in chemical composition and viscosity. For example, α-pinene SOM viscosity from the OFR experiments in S. Petters et al. (2019) show a difference in 16°C for the estimated $T_g$. Reasons for the discrepancy are a combination of mass loading effects, errors from the extrapolation of the measured transition to $T_g$, and differences in chemical composition. As summarized in S. Petters et al. (2019), differences by a few 10 s °C in the observed viscosity transition (and by extension $T_g$) can be due to differences in functional group composition or small differences in the average molecular weight of the SOM. An upside of this natural variability in aerosol properties is that repeat ice nucleation experiments from multiple studies test the influence of this variability on ice nucleation, thus strengthening the conclusion that these differences in composition do not affect the main conclusion that SOM particles are important heterogeneous INP. Many IN data points cluster above the Koop et al. (2000) prediction for homogeneous freezing, further suggesting that these particles do not easily liquefy into haze droplets under those conditions. In fact, some of the OFR generated aerosols from this study appear to be so hydrophobic that droplet activation followed by freezing is not observed even under water supersaturated conditions (Figure 8).

Particles that do liquefy are expected to freeze near the homogenous freezing limit. This is observed by some pure SOM summarized in Figures 6 and 7 and SOM (α-pinene/$O_3$) coated ammonium sulfate particles in previous

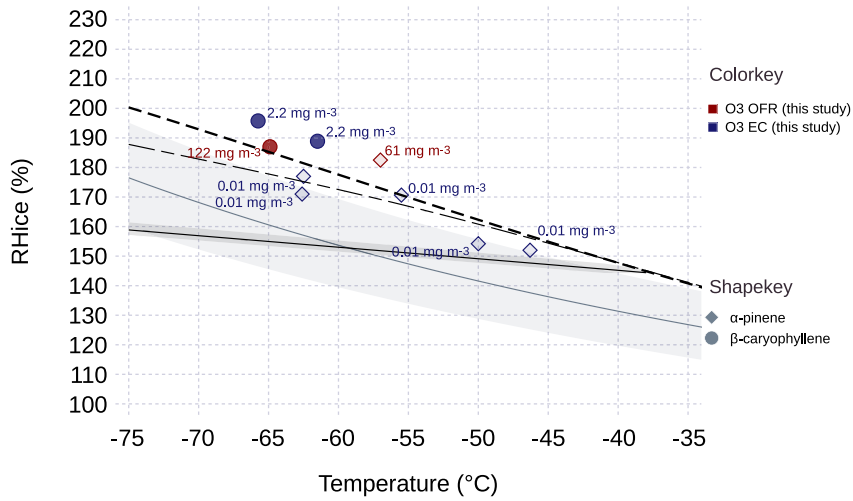


**Figure 9.** Summary of experiments E1, E3, E10, and E18 for α-pinene and β-caryophyllene. Annotations denote the estimated mass loading. Lines, symbols, and shadings are as in Figure 7.

studies (Bertozzi et al., 2021; Ladino et al., 2014; Wagner et al., 2017). Möhler et al. (2008) and recently Bertozzi et al. (2021), studied SOM-generated α-pinene/$O_3$ particles with internal mixtures of ammonium sulfate (AS) and soot where the ability of heterogeneous IN of AS and soot particles is suppressed by the SOM coating materials.

To better understand how potential differences in particle generation pathways affect IN we contrasted high (∼61 and ∼122 mg $m^{-3}$ for α-pinene/$O_3$ and β-caryophyllene/$O_3$, respectively) and low mass loadings (∼0.01 and ∼2.2 mg $m^{-3}$ for α-pinene/$O_3$ and β-caryophyllene/$O_3$, respectively) for α-pinene/$O_3$ and β-caryophyllene/$O_3$ derived SOM (see Figure 9). Similar IN results were observed for β-caryophyllene/$O_3$ derived SOM from the OFR and EC, neither of which showed freezing below water saturation. The α-pinene/$O_3$ experiments were designed to explore the potential role of more oxidized compounds that form via the autooxidation pathway. This pathway is prevalent at low precursor mass concentration. For the α-pinene/$O_3$ experiment (E18) (∼0.01 mg $m^{-3}$ mass loading based on mean volume concentration with a unit density assumption) these products are expected to have higher O:C ratios and higher-molecular-weight products than the SOM generated at high mass concentration as seen in E3 (∼61 mg $m^{-3}$ mass loading based on mean volume concentration with a unit density assumption) (Claflin et al., 2018). In contrast to the particles derived from α-pinene/$O_3$ in the OFR at high mass concentration, which did not show freezing below water saturation, the particles generated at low mass concentration in the EC froze consistent with the homogeneous nucleation threshold. This suggests that the products are water soluble and/or liquid at those conditions.

The experiments here were performed without any inorganic seed particles. The use of seed particles in secondary organic aerosol generation studies, however, is common (e.g., Wong et al., 2015). The presence of seed particles may affect the results through different mechanisms. Acidic seeds present during the initial generation may lead to acid catalyzed reactions (Piedehierro et al., 2021), which in turn would change the chemical composition of the SOM. Chemically inert deliquescent seeds may take up water prior to reaching the homogenous freezing limit. For coated particles we would expect that water can diffuse through an organic shell (Tandon et al., 2019), resulting in liquefaction of the particles. This water uptake is expected to shift observation from above the homogenous freezing limit closer toward the homogeneous freezing limit. Finally, solid IN active seeds might induce heterogeneous freezing nucleation if active sites are exposed. However, complete coatings appear to shield such particles from nucleating ice below the homogeneous freezing threshold (Bertozzi et al., 2021; Koehler et al., 2010; Möhler et al., 2008). The results summarized in Figure 6 include studies with ice nucleating active seeds SOM coated dust particles in Koehler et al. (2010) and illite as seed particles in Möhler et al. (2008) and ammonium sulfate as an acidic seed particles in Piedehierro et al. (2021).

We were also interested in the potential effect of SOM with less-well explored functional group composition on IN. We therefore performed experiments with β-pinene that reacted with $NO_3$. The reaction produces SOM including acetal heterodimers and heterotrimers with $–ONO_2$ moieties attached (Claflin & Ziemann, 2018).

Unfortunately, the reaction did not produce enough aerosol to measure the viscosity or volatility. The data show that freezing required conditions in excess of water saturation, suggesting that the compounds are either viscous or hydrophobic, or both. This is consistent with the fact that the dominant products are expected to be dimers and trimers with two and three $–ONO_2$ groups (Claflin & Ziemann, 2018), with our general understanding that viscosity increases with molecular weight (Rothfuss & Petters, 2017b) and with our understanding that organic $–ONO_2$ moieties tend to reduce solubility in water and in turn hygroscopicity (Suda et al., 2014).

Finally, we were interested in the potential effect of SOM with molecular structures that resemble those of known organic INP, specifically phloroglucinol. Phloroglucinol is a 1,3,5-benzenetriol and promotes IN (Langer et al., 1978). Here we used resorcinol/OH and catechol/Cl and catechol/OH as SOM precursors. Phloroglucinol has one more diol group in its structure when compared to resorcinol (1,3-benzenediol) and catechol. Finewax et al. (2018, 2019) showed that catechol/OH, and resorcinol/OH produce particles. Dominant particle-phase products formed include benzenetriol, nitrobenzenetriol, 4-nitrocatechol, and 4-nitroresorcinol. Results from our experiments with these compounds (E5, E9, and E15 in Table 1, Figure 8) showed that freezing onset is observed near or above the water saturation line. This again suggests that the products are either viscous, hydrophobic, or both. Thus, despite the similarity in molecular structure, these products did not promote ice formation. This is similar to the finding of Prenni et al. (2009), who investigated the potential IN activity of aerosol produced from reactions of linear alkenes with $O_3$ at −30°C in the immersion mode. In their experiments the products mimic the molecular structure of aliphatic long-chain alcohols, which can nucleate ice when arranged as a monolayer on liquid droplets (Gavish et al., 1990). Both Prenni et al. (2009) and this study suggest that these structural similarities are not sufficient to predict IN activity.

An important question is whether the vertical level of SOM formation in the atmosphere may behave differently from the proxies studied here. SOM formed at colder temperature may differ in O:C ratio and dimer fraction (e.g., Kristensen et al., 2017). However, based on our findings, moderate chemical differences in complex SOM are not important for predicting ice nucleation activity. Therefore SOM formation near the surface or SOMs forming aloft are likely equally poor heterogeneous INP.

Our results are limited to $T > -60$°C. However, temperatures in the upper troposphere may be as low as −80°C. Based on our experimental results, and the assertion that many of the SOMs are hydrophobic and glassy at $T < -10$°C, we do not expect that any of the SOMs discussed here would serve as heterogeneous nuclei at colder temperatures. It is however possible that some of the systems that showed activity closer to the homogeneous freezing limit did form aqueous haze drops and it would be possible in principle for those systems to transform into heterogeneous INP similar to what is observed for pure compounds such as citric acid.

## 5. Conclusions

The combination of INP measurements at $T < -40$°C, viscosity, and volatility measurements are reported for the SOM generated from the oxidation of terpenes (both monoterpenes and sesquiterpenes) and aromatic precursors. $T_g$ was found by extrapolation and ranged between 9.9 and 21.9°C. We confirmed that SOM generated from $\Delta^3$-carene/$O_3$ remained viscous at $T$/RH and residence time in the CFDC. The volume fraction remaining of the generated SOM was between 0.82 and 0.96 at ∼45°C and similar for OFR (high SOM loadings) and EC (lower SOM loading) experiments. Based on known correlation between volatility and viscosity (Champion et al., 2019; Li et al., 2020), we expect that the particles generated in the EC were at least as viscous as those generated in the OFR. No heterogeneous IN was observed for any of the particles generated in this study. Many of the systems required conditions above the homogeneous freezing limit or above water saturation to freeze, thus corroborating that the particles were either viscous, hydrophobic or both. A glassy phase state may be necessary but is not a sufficient criterion for particles to freeze heterogeneously. Experiments exploring a wide range of functional groups and mass loadings did not reveal any obvious influence of particle chemistry or generation conditions on the CFDC results. Neither $–ONO_2$ groups nor high-molecular weight compounds from autoxidation promoted ice nucleation. Close structural matches between the known organic INP phloroglucinol and SOM from the precursors resorcinol/OH, catechol/Cl and catechol/OH did not produce particles that promoted freezing. Collating similar laboratory data across multiple studies suggests that complex SOM is unlikely to significantly contribute to the heterogeneous INP population in the upper free troposphere. It is thus recommended to treat glassy or liquid SOM and dust coated with glassy or liquid SOM in models as IN inactive.

## Data Availability Statement

All data and scripts used to create the figures in work are archived on Zenodo which could be find at: [Data] and [Software] (Kasparoglu et al., 2022). Data—Ice nucleating particle concentrations were measured using Colorado State University low temperature continuous flow diffusion chamber (CFDC). Environmental chamber (EC) of the University of Colorado, Boulder was used to generate secondary organic material. The rest of the instruments used to perform experiments were from North Carolina State University and they temporarily moved to the University of Colorado, Boulder. Software—Postprocessing and figures were made with Julia Language (Bezanson et al., 2017).

**Acknowledgments**
This research was supported with funds from the US Department of Energy grant DE-SC0018265.

## References

Ansmann, A., Mamouri, R.-E., Bühl, J., Seifert, P., Engelmann, R., Hofer, J., et al. (2019). Ice-nucleating particle versus ice crystal number concentration in altocumulus and cirrus layers embedded in Saharan dust: A closure study. *Atmospheric Chemistry and Physics*, *19*(23), 15087–15115. https://doi.org/10.5194/acp-19-15087-2019

Archuleta, C. M., DeMott, P. J., & Kreidenweis, S. M. (2005). Ice nucleation by surrogates for atmospheric mineral dust and mineral dust/sulfate particles at cirrus temperatures. *Atmospheric Chemistry and Physics*, *5*(10), 2617–2634. https://doi.org/10.5194/acp-5-2617-2005

Baumgartner, M., Rolf, C., Grooß, J.-U., Schneider, J., Schorr, T., Möhler, O., et al. (2022). New investigations on homogeneous ice nucleation: The effects of water activity and water saturation formulations. *Atmospheric Chemistry and Physics*, *22*(1), 65–91. https://doi.org/10.5194/acp-22-65-2022

Baustian, K. J., Wise, M. E., Jensen, E. J., Schill, G. P., Freedman, M. A., & Tolbert, M. A. (2013). State transformations and ice nucleation in amorphous (semi-)solid organic aerosol. *Atmospheric Chemistry and Physics*, *13*(11), 5615–5628. https://doi.org/10.5194/acp-13-5615-2013

Berkemeier, T., Shiraiwa, M., Pöschl, U., & Koop, T. (2014). Competition between water uptake and ice nucleation by glassy organic aerosol particles. *Atmospheric Chemistry and Physics*, *14*(22), 12513–12531. https://doi.org/10.5194/acp-14-12513-2014

Bertozzi, B., Wagner, R., Song, J., Höhler, K., Pfeifer, J., Saathoff, H., et al. (2021). Ice nucleation ability of ammonium sulfate aerosol particles internally mixed with secondary organics. *Atmospheric Chemistry and Physics*, *21*(13), 10779–10798. https://doi.org/10.5194/acp-21-10779-2021

Bezanson, J., Edelman, A., Karpinski, S., & Shah, V. B. (2017). Julia: A fresh approach to numerical computing. *SIAM Review*, *59*(1), 65–98. https://doi.org/10.1137/141000671

Bilde, M., Barsanti, K., Booth, M., Cappa, C. D., Donahue, N. M., Emanuelsson, E. U., et al. (2015). Saturation vapor pressures and transition enthalpies of low-volatility organic molecules of atmospheric relevance: From dicarboxylic acids to complex mixtures. *Chemical Reviews*, *115*(10), 4115–4156. https://doi.org/10.1021/cr5005502

Buck, A. L. (1981). New equations for computing vapor pressure and enhancement factor. *Journal of Applied Meteorology*, *20*(12), 1527–1532. https://doi.org/10.1175/1520-0450(1981)020<1527:NEFCVP>2.0.CO;2

Buck Research Instruments, LLC. (2010). *Model CR-1A Hygrometer with autofill: Operating manual*. Buck Research Instruments, LLC. Retrieved from http://www.hygrometers.com/wp-content/uploads/CR-1A-users-manual-2009-12.pdf

Burtscher, H., Baltensperger, U., Bukowiecki, N., Cohn, P., Hüglin, C., Mohr, M., et al. (2001). Separation of volatile and non-volatile aerosol fractions by thermodesorption: Instrumental development and applications. *Journal of Aerosol Science*, *32*(4), 427–442. https://doi.org/10.1016/S0021-8502(00)00089-6

Campbell, J. M., Meldrum, F. C., & Christenson, H. K. (2017). Observing the formation of ice and organic crystals in active sites. *Proceedings of the National Academy of Sciences*, *114*(5), 810–815. https://doi.org/10.1073/pnas.1617717114

Champion, W. M., Rothfuss, N. E., Petters, M. D., & Grieshop, A. P. (2019). Volatility and viscosity are correlated in terpene secondary organic aerosol formed in a flow reactor. *Environmental Science and Technology Letters*, *6*(9), 513–519. https://doi.org/10.1021/acs.estlett.9b00412

Charnawskas, J. C., Alpert, P. A., Lambe, A. T., Berkemeier, T., O'Brien, R. E., Massoli, P., et al. (2017). Condensed-phase biogenic–anthropogenic interactions with implications for cold cloud formation. *Faraday Discussions*, *200*, 165–194. https://doi.org/10.1039/C7FD00010C

Chen, Y., DeMott, P. J., Kreidenweis, S. M., Rogers, D. C., & Sherman, D. E. (2000). Ice Formation by sulfate and sulfuric acid aerosol particles under upper-tropospheric conditions. *Journal of the Atmospheric Sciences*, *57*(22), 3752–3766. https://doi.org/10.1175/1520-0469(2000)057<3752:IFBSAS>2.0.CO;2

Chen, Y., Kreidenweis, S. M., McInnes, L. M., Rogers, D. C., & DeMott, P. J. (1998). Single particle analyses of ice nucleating aerosols in the upper troposphere and lower stratosphere. *Geophysical Research Letters*, *25*(9), 1391–1394. https://doi.org/10.1029/97GL03261

Claflin, M. S., Krechmer, J. E., Hu, W., Jimenez, J. L., & Ziemann, P. J. (2018). Functional group composition of secondary organic aerosol formed from ozonolysis of α-pinene under high VOC and autoxidation conditions. *ACS Earth and Space Chemistry*, *2*(11), 1196–1210. https://doi.org/10.1021/acsearthspacechem.8b00117

Claflin, M. S., & Ziemann, P. J. (2018). Identification and quantitation of aerosol products of the reaction of β-pinene with $NO_3$ radicals and implications for gas- and particle-phase reaction mechanisms. *The Journal of Physical Chemistry A*, *122*(14), 3640–3652. https://doi.org/10.1021/acs.jpca.8b00692

Cziczo, D. J., & Froyd, K. D. (2014). Sampling the composition of cirrus ice residuals. *Atmospheric Research*, *142*, 15–31. https://doi.org/10.1016/j.atmosres.2013.06.012

Cziczo, D. J., Ladino, L., Boose, Y., Kanji, Z. A., Kupiszewski, P., Lance, S., et al. (2017). Measurements of ice nucleating particles and ice residuals. *Meteorological Monographs*, *58*, 8.1–8.13. https://doi.org/10.1175/AMSMONOGRAPHS-D-16-0008.1

David, R. O., Marcolli, C., Fahrni, J., Qiu, Y., Perez Sirkin, Y. A., Molinero, V., et al. (2019). Pore condensation and freezing is responsible for ice formation below water saturation for porous particles. *Proceedings of the National Academy of Sciences*, *116*(17), 8184–8189. https://doi.org/10.1073/pnas.1813647116

Davies, J. F., & Wilson, K. R. (2016). Raman spectroscopy of isotopic water diffusion in ultraviscous, glassy, and gel states in aerosol by use of optical tweezers. *Analytical Chemistry*, *88*(4), 2361–2366. https://doi.org/10.1021/acs.analchem.5b04315

DeMott, P. J., Cziczo, D. J., Prenni, A. J., Murphy, D. M., Kreidenweis, S. M., Thomson, D. S., et al. (2003). Measurements of the concentration and composition of nuclei for cirrus formation. *Proceedings of the National Academy of Sciences*, *100*(25), 14655–14660. https://doi.org/10.1073/pnas.2532677100

DeMott, P. J., Petters, M. D., Prenni, A. J., Carrico, C. M., Kreidenweis, S. M., Collett, J. L., Jr., & Moosmüller, H. (2009). Ice nucleation behavior of biomass combustion particles at cirrus temperatures. *Journal of Geophysical Research*, *114*(D16), D16205. https://doi.org/10.1029/2009JD012036

DeMott, P. J., Prenni, A. J., Liu, X., Kreidenweis, S. M., Petters, M. D., Twohy, C. H., et al. (2010). Predicting global atmospheric ice nuclei distributions and their impacts on climate. *Proceedings of the National Academy of Sciences*, *107*(25), 11217–11222. https://doi.org/10.1073/pnas.0910818107

DeMott, P. J., Prenni, A. J., McMeeking, G. R., Sullivan, R. C., Petters, M. D., Tobo, Y., et al. (2015). Integrating laboratory and field data to quantify the immersion freezing ice nucleation activity of mineral dust particles. *Atmospheric Chemistry and Physics*, *15*(1), 393–409. https://doi.org/10.5194/acp-15-393-2015

Donahue, N. M., Robinson, A. L., & Pandis, S. N. (2009). Atmospheric organic particulate matter: From smoke to secondary organic aerosol. *Atmospheric Environment*, *43*(1), 94–106. https://doi.org/10.1016/j.atmosenv.2008.09.055

Durant, A. J., & Shaw, R. A. (2005). Evaporation freezing by contact nucleation inside-out. *Geophysical Research Letters*, *32*(20), L20814. https://doi.org/10.1029/2005GL024175

Faulhaber, A. E., Thomas, B. M., Jimenez, J. L., Jayne, J. T., Worsnop, D. R., & Ziemann, P. J. (2009). Characterization of a thermodenuder-particle beam mass spectrometer system for the study of organic aerosol volatility and composition. *Atmospheric Measurement Techniques*, *2*(1), 15–31. https://doi.org/10.5194/amt-2-15-2009

Finewax, Z., de Gouw, J. A., & Ziemann, P. J. (2018). Identification and quantification of 4-nitrocatechol formed from OH and $NO_3$ radical-initiated reactions of catechol in air in the presence of $NO_x$: Implications for secondary organic aerosol formation from biomass burning. *Environmental Science & Technology*, *52*(4), 1981–1989. https://doi.org/10.1021/acs.est.7b05864

Finewax, Z., de Gouw, J. A., & Ziemann, P. J. (2019). Products and secondary organic aerosol yields from the OH and $NO_3$ radical-initiated oxidation of resorcinol. *ACS Earth and Space Chemistry*, *3*(7), 1248–1259. https://doi.org/10.1021/acsearthspacechem.9b00112

Fulcher, G. S. (1925). Analysis of recent measurements of the viscosity of glasses. *Journal of the American Ceramic Society*, *8*(6), 339–355. https://doi.org/10.1111/j.1151-2916.1925.tb16731.x

Gavish, M., Popovitz-Biro, R., Lahav, M., & Leiserowitz, L. (1990). Ice nucleation by alcohols arranged in monolayers at the surface of water drops. *Science*, *250*(4983), 973–975. https://doi.org/10.1126/science.250.4983.973

Grayson, J. W., Zhang, Y., Mutzel, A., Renbaum-Wolff, L., Böge, O., Kamal, S., et al. (2016). Effect of varying experimental conditions on the viscosity of α-pinene derived secondary organic material. *Atmospheric Chemistry and Physics*, *16*(10), 6027–6040. https://doi.org/10.5194/acp-16-6027-2016

Gu, S., Guenther, A., & Faiola, C. (2021). Effects of anthropogenic and biogenic volatile organic compounds on Los Angeles air quality. *Environmental Science & Technology*, *55*(18), 12191–12201. https://doi.org/10.1021/acs.est.1c01481

Guenther, A. B., Jiang, X., Heald, C. L., Sakulyanontvittaya, T., Duhl, T., Emmons, L. K., & Wang, X. (2012). The model of emissions of gases and aerosols from nature version 2.1 (MEGAN2.1): An extended and updated framework for modeling biogenic emissions. *Geoscientific Model Development*, *5*(6), 1471–1492. https://doi.org/10.5194/gmd-5-1471-2012

Hallquist, M., Wenger, J. C., Baltensperger, U., Rudich, Y., Simpson, D., Claeys, M., et al. (2009). The formation, properties and impact of secondary organic aerosol: Current and emerging issues. *Atmospheric Chemistry and Physics*, *9*(14), 5155–5236. https://doi.org/10.5194/acp-9-5155-2009

Heymsfield, A. J., Krämer, M., Luebke, A., Brown, P., Cziczo, D. J., Franklin, C., et al. (2017). Cirrus clouds. *Meteorological Monographs*, *58*, 2.1–2.26. https://doi.org/10.1175/AMSMONOGRAPHS-D-16-0010.1

Hiranuma, N., Hoffmann, N., Kiselev, A., Dreyer, A., Zhang, K., Kulkarni, G., et al. (2014). Influence of surface morphology on the immersion mode ice nucleation efficiency of hematite particles. *Atmospheric Chemistry and Physics*, *14*(5), 2315–2324. https://doi.org/10.5194/acp-14-2315-2014

Hoose, C., & Möhler, O. (2012). Heterogeneous ice nucleation on atmospheric aerosols: A review of results from laboratory experiments. *Atmospheric Chemistry and Physics*, *12*(20), 9817–9854. https://doi.org/10.5194/acp-12-9817-2012

Huffman, J. A., Ziemann, P. J., Jayne, J. T., Worsnop, D. R., & Jimenez, J. L. (2008). Development and characterization of a fast-stepping/scanning thermodenuder for chemically-resolved aerosol volatility measurements. *Aerosol Science and Technology*, *42*(5), 395–407. https://doi.org/10.1080/02786820802104981

Ignatius, K., Kristensen, T. B., Järvinen, E., Nichman, L., Fuchs, C., Gordon, H., et al. (2016). Heterogeneous ice nucleation of viscous secondary organic aerosol produced from ozonolysis of α-pinene. *Atmospheric Chemistry and Physics*, *16*(10), 6495–6509. https://doi.org/10.5194/acp-16-6495-2016

Ingram, S., Cai, C., Song, Y.-C., Glowacki, D. R., Topping, D. O., O'Meara, S., & Reid, J. P. (2017). Characterising the evaporation kinetics of water and semi-volatile organic compounds from viscous multicomponent organic aerosol particles. *Physical Chemistry Chemical Physics*, *19*(47), 31634–31646. https://doi.org/10.1039/C7CP05172G

Junge, C. H. R. (1953). Die Rolle der Aerosole und der gasförmigen Beimengungen der Luft im Spurenstoffhaushalt der Troposphäre. *Tellus*, *5*(1), 1–26. https://doi.org/10.1111/j.2153-3490.1953.tb01031.x

Kanji, Z. A., Ladino, L. A., Wex, H., Boose, Y., Burkert-Kohn, M., Cziczo, D. J., & Krämer, M. (2017). Overview of ice nucleating particles. *Meteorological Monographs*, *58*, 1.1–1.33. https://doi.org/10.1175/AMSMONOGRAPHS-D-16-0006.1

Kasparoglu, S., Li, Y., Shiraiwa, M., & Petters, M. D. (2021). Toward closure between predicted and observed particle viscosity over a wide range of temperatures and relative humidity. *Atmospheric Chemistry and Physics*, *21*(2), 1127–1141. https://doi.org/10.5194/acp-21-1127-2021

Kasparoglu, S., Perkins, R., Ziemann, P. J., DeMott, P. J., Kreidenweis, S. M., Finewax, Z., et al. (2022). Dataset for "Experimental determination of the relationship between organic aerosol viscosity and ice nucleation at upper free tropospheric conditions" (Version 1.0) [Dataset]. Zenodo. https://doi.org/10.5281/ZENODO.6547307

Kasparoglu, S., Wright, T. P., & Petters, M. D. (2022). Open-hardware design and characterization of an electrostatic aerosol precipitator. *HardwareX*, *11*, e00266. https://doi.org/10.1016/j.ohx.2022.e00266

Kilchhofer, K., Mahrt, F., & Kanji, Z. A. (2021). The role of cloud processing for the ice nucleating ability of organic aerosol and coal fly ash particles. *Journal of Geophysical Research: Atmospheres*, *126*(10), e2020JD033338. https://doi.org/10.1029/2020JD033338

Knopf, D. A., Alpert, P. A., & Wang, B. (2018). The role of organic aerosol in atmospheric ice nucleation: A review. *ACS Earth and Space Chemistry*, *2*(3), 168–202. https://doi.org/10.1021/acsearthspacechem.7b00120

Koehler, K. A., Kreidenweis, S. M., DeMott, P. J., Petters, M. D., Prenni, A. J., & Möhler, O. (2010). Laboratory investigations of the impact of mineral dust aerosol on cold cloud formation. *Atmospheric Chemistry and Physics*, *10*(23), 11955–11968. https://doi.org/10.5194/acp-10-11955-2010

Kolesar, K. R., Chen, C., Johnson, D., & Cappa, C. D. (2015). The influences of mass loading and rapid dilution of secondary organic aerosol on particle volatility. *Atmospheric Chemistry and Physics*, *15*(16), 9327–9343. https://doi.org/10.5194/acp-15-9327-2015

Koop, T., Bookhold, J., Shiraiwa, M., & Pöschl, U. (2011). Glass transition and phase state of organic compounds: Dependency on molecular properties and implications for secondary organic aerosols in the atmosphere. *Physical Chemistry Chemical Physics*, *13*(43), 19238–19255. https://doi.org/10.1039/C1CP22617G

Koop, T., Luo, B., Tsias, A., & Peter, T. (2000). Water activity as the determinant for homogeneous ice nucleation in aqueous solutions. *Nature*, *406*(6796), 611–614. https://doi.org/10.1038/35020537

Kreidenweis, S. M., Petters, M. D., & Chuang, P. Y. (2009). Cloud particle precursors. In *Clouds in the Perturbed Climate System*. The MIT Press. https://doi.org/10.7551/mitpress/9780262012874.003.0013

Kristensen, K., Jensen, L. N., Glasius, M., & Bilde, M. (2017). The effect of sub-zero temperature on the formation and composition of secondary organic aerosol from ozonolysis of alpha-pinene. *Environmental Science: Processes & Impacts*, *19*(10), 1220–1234. https://doi.org/10.1039/C7EM00231A

Ladino, L. A., Yakobi-Hancock, J. D., Kilthau, W. P., Mason, R. H., Si, M., Li, J., et al. (2016). Addressing the ice nucleating abilities of marine aerosol: A combination of deposition mode laboratory and field measurements. *Atmospheric Environment*, *132*, 1–10. https://doi.org/10.1016/j.atmosenv.2016.02.028

Ladino, L. A., Zhou, S., Yakobi-Hancock, J. D., Aljawhary, D., & Abbatt, J. P. D. (2014). Factors controlling the ice nucleating abilities of $\alpha$-pinene SOA particles. *Journal of Geophysical Research: Atmospheres*, *119*(14), 9041–9051. https://doi.org/10.1002/2014JD021578

Langer, G., Cooper, G., Nagamoto, C. T., & Rosinski, J. (1978). Ice nucleation mechanisms of submicron monodispersed silver iodide, 1, 5-dihydroxynaphthalene and phloroglucinol aerosol particles. *Journal of Applied Meteorology and Climatology*, *17*(7), 1039–1048. https://doi.org/10.1175/1520-0450(1978)017<1039:inmosm>2.0.co;2

Levin, E. J. T., McMeeking, G. R., DeMott, P. J., McCluskey, C. S., Carrico, C. M., Nakao, S., et al. (2016). Ice-nucleating particle emissions from biomass combustion and the potential importance of soot aerosol. *Journal of Geophysical Research: Atmospheres*, *121*(10), 5888–5903. https://doi.org/10.1002/2016JD024879

Li, Y., Day, D. A., Stark, H., Jimenez, J. L., & Shiraiwa, M. (2020). Predictions of the glass transition temperature and viscosity of organic aerosols from volatility distributions. *Atmospheric Chemistry and Physics*, *20*(13), 8103–8122. https://doi.org/10.5194/acp-20-8103-2020

Lienhard, D. M., Huisman, A. J., Krieger, U. K., Rudich, Y., Marcolli, C., Luo, B. P., et al. (2015). Viscous organic aerosol particles in the upper troposphere: Diffusivity-controlled water uptake and ice nucleation? *Atmospheric Chemistry and Physics*, *15*(23), 13599–13613. https://doi.org/10.5194/acp-15-13599-2015

Mahata, P. C., & Alofs, D. J. (1975). Insoluble condensation nuclei: The effect of contact angle, surface roughness and adsorption. *Journal of the Atmospheric Sciences*, *32*(1), 116–122. https://doi.org/10.1175/1520-0469(1975)032<0116:ICNTEO>2.0.CO;2

Marcolli, C. (2014). Deposition nucleation viewed as homogeneous or immersion freezing in pores and cavities. *Atmospheric Chemistry and Physics*, *14*(4), 2071–2104. https://doi.org/10.5194/acp-14-2071-2014

Marsh, A., Petters, S. S., Rothfuss, N. E., Rovelli, G., Song, Y. C., Reid, J. P., & Petters, M. D. (2018). Amorphous phase state diagrams and viscosity of ternary aqueous organic/organic and inorganic/organic mixtures. *Physical Chemistry Chemical Physics*, *20*(22), 15086–15097. https://doi.org/10.1039/C8CP00760H

Mendes, L., Eleftheriadis, K., & Biskos, G. (2016). Performance comparison of two thermodenuders in Volatility Tandem DMA measurements. *Journal of Aerosol Science*, *92*, 38–52. https://doi.org/10.1016/j.jaerosci.2015.10.002

Möhler, O., Benz, S., Saathoff, H., Schnaiter, M., Wagner, R., Schneider, J., et al. (2008). The effect of organic coating on the heterogeneous ice nucleation efficiency of mineral dust aerosols. *Environmental Research Letters*, *3*(2), 025007. https://doi.org/10.1088/1748-9326/3/2/025007

Murphy, D. M., & Koop, T. (2005). Review of the vapour pressures of ice and supercooled water for atmospheric applications. *Quarterly Journal of the Royal Meteorological Society*, *131*(608), 1539–1565. https://doi.org/10.1256/qj.04.94

Murray, B. J., Wilson, T. W., Dobbie, S., Cui, Z., Al-Jumur, S. M. R. K., Möhler, O., et al. (2010). Heterogeneous nucleation of ice particles on glassy aerosols under cirrus conditions. *Nature Geoscience*, *3*(4), 233–237. https://doi.org/10.1038/ngeo817

Odum, J. R., Hoffmann, T., Bowman, F., Collins, D., Flagan, R. C., & Seinfeld, J. H. (1996). Gas/particle partitioning and secondary organic aerosol yields. *Environmental Science & Technology*, *30*(8), 2580–2585. https://doi.org/10.1021/es950943+

Oxford, C. R., Dang, A. J., Rapp, C. M., & Williams, B. J. (2020). Interpretation of Volatility Tandem Differential Mobility Analyzer (V-TDMA) data for accurate vapor pressure and enthalpy measurement: Operational considerations, multiple charging, and introduction to a new analysis program (TAO). *Aerosol Science and Technology*, *54*(4), 410–425. https://doi.org/10.1080/02786826.2019.1709617

Pankow, J. F. (1994). An absorption model of the gas/aerosol partitioning involved in the formation of secondary organic aerosol. *Atmospheric Environment*, *28*(2), 189–193. https://doi.org/10.1016/1352-2310(94)90094-9

Patnaude, R. J., Perkins, R. J., Kreidenweis, S. M., & DeMott, P. J. (2021). Is ice formation by sea spray particles at cirrus temperatures controlled by crystalline salts? *ACS Earth and Space Chemistry*, *5*(9), 2196–2211. https://doi.org/10.1021/acsearthspacechem.1c00228

Petters, M. D. (2018). A language to simplify computation of differential mobility analyzer response functions. *Aerosol Science and Technology*, *52*(12), 1437–1451. https://doi.org/10.1080/02786826.2018.1530724

Petters, M. D., & Kreidenweis, S. M. (2007). A single parameter representation of hygroscopic growth and cloud condensation nucleus activity. *Atmospheric Chemistry and Physics*, *7*(8), 1961–1971. https://doi.org/10.5194/acp-7-1961-2007

Petters, S., Kreidenweis, S. M., Grieshop, A. P., Ziemann, P. J., & Petters, M. D. (2019). Temperature- and humidity-dependent phase states of secondary organic aerosols. *Geophysical Research Letters*, *46*(2), 1005–1013. https://doi.org/10.1029/2018GL080563

Piedehierro, A. A., Welti, A., Buchholz, A., Korhonen, K., Pullinen, I., Summanen, I., et al. (2021). Ice nucleation on surrogates of boreal forest SOA particles: Effect of water content and oxidative age. *Atmospheric Chemistry and Physics*, *21*(14), 11069–11078. https://doi.org/10.5194/acp-21-11069-2021

Pokluda, O., Bellehumeur, C. T., & Vlachopoulos, J. (1997). Modification of Frenkel's model for sintering. *AIChE Journal*, *43*(12), 3253–3256. https://doi.org/10.1002/aic.690431213

Prenni, A. J., Petters, M. D., Faulhaber, A., Carrico, C. M., Ziemann, P. J., Kreidenweis, S. M., & DeMott, P. J. (2009). Heterogeneous ice nucleation measurements of secondary organic aerosol generated from ozonolysis of alkenes. *Geophysical Research Letters*, *36*(6), L06808. https://doi.org/10.1029/2008GL036957

Rader, D. J., McMurry, P. H., & Smith, S. (1987). Evaporation rates of monodisperse organic aerosols in the 0.02- to 0.2-μm-diameter range. *Aerosol Science and Technology*, *6*(3), 247–260. https://doi.org/10.1080/02786828708959137

Reid, J. P., Bertram, A. K., Topping, D. O., Laskin, A., Martin, S. T., Petters, M. D., et al. (2018). The viscosity of atmospherically relevant organic particles. *Nature Communications*, *9*(1), 956. https://doi.org/10.1038/s41467-018-03027-z

Richardson, M. (2009). *Making real time measurements of ice nuclei concentrations at upper tropospheric temperatures: Extending the capabilities of the continuous flow diffusion chamber* (Ph.D.). ProQuest Dissertations and Theses. Colorado State University. Retrieved from https://www.proquest.com/dissertations-theses/making-real-time-measurements-ice-nuclei/docview/304863199/se-2?accountid=14472

Rosinski, J., Kopcewicz, B., & Sandoval, N. (1990). Heterogeneous nucleation of ice at the liquid-liquid interface. *Journal of Aerosol Science*, *21*(1), 87–96. https://doi.org/10.1016/0021-8502(90)90025-S

Rothfuss, N. E., & Petters, M. D. (2016). Coalescence-based assessment of aerosol phase state using dimers prepared through a dual-differential mobility analyzer technique. *Aerosol Science and Technology*, *50*(12), 1294–1305. https://doi.org/10.1080/02786826.2016.1221050

Rothfuss, N. E., & Petters, M. D. (2017a). Characterization of the temperature and humidity-dependent phase diagram of amorphous nanoscale organic aerosols. *Physical Chemistry Chemical Physics*, *19*(9), 6532–6545. https://doi.org/10.1039/C6CP08593H

Rothfuss, N. E., & Petters, M. D. (2017b). Influence of functional groups on the viscosity of organic aerosol. *Environmental Science & Technology*, *51*(1), 271–279. https://doi.org/10.1021/acs.est.6b04478

Rothfuss, N. E., Petters, S. S., Champion, W. M., Grieshop, A. P., & Petters, M. D. (2019). Characterization of a dimer preparation method for nanoscale organic aerosol. *Aerosol Science and Technology*, *39*(9), 998–1011. https://doi.org/10.1080/02786826.2019.1623379

Saha, P. K., & Grieshop, A. P. (2016). Exploring divergent volatility properties from yield and thermodenuder measurements of secondary organic aerosol from α-pinene ozonolysis. *Environmental Science & Technology*, *50*(11), 5740–5749. https://doi.org/10.1021/acs.est.6b00303

Sakulyanontvittaya, T., Guenther, A., Helmig, D., Milford, J., & Wiedinmyer, C. (2008). Secondary organic aerosol from sesquiterpene and monoterpene emissions in the United States. *Environmental Science & Technology*, *42*(23), 8784–8790. https://doi.org/10.1021/es800817r

Schill, G. P., & Tolbert, M. A. (2014). Heterogeneous ice nucleation on simulated sea-spray aerosol using Raman microscopy. *Journal of Physical Chemistry C*, *118*(50), 29234–29241. https://doi.org/10.1021/jp505379j

Schneider, J., Höhler, K., Wagner, R., Saathoff, H., Schnaiter, M., Schorr, T., et al. (2021). High homogeneous freezing onsets of sulfuric acid aerosol at cirrus temperatures. *Atmospheric Chemistry and Physics*, *21*(18), 14403–14425. https://doi.org/10.5194/acp-21-14403-2021

Shaw, S. L., Gantt, B., & Meskhidze, N. (2010). Production and emissions of marine isoprene and monoterpenes: A review. *Advances in Meteorology*, *2010*, 1–24. https://doi.org/10.1155/2010/408696

Shilling, J. E., Zaveri, R. A., Fast, J. D., Kleinman, L., Alexander, M. L., Canagaratna, M. R., et al. (2013). Enhanced SOA formation from mixed anthropogenic and biogenic emissions during the CARES campaign. *Atmospheric Chemistry and Physics*, *13*(4), 2091–2113. https://doi.org/10.5194/acp-13-2091-2013

Storelvmo, T., & Herger, N. (2014). Cirrus cloud susceptibility to the injection of ice nuclei in the upper troposphere. *Journal of Geophysical Research: Atmospheres*, *119*(5), 2375–2389. https://doi.org/10.1002/2013JD020816

Suda, S. R., Petters, M. D., Yeh, G. K., Strollo, C., Matsunaga, A., Faulhaber, A., et al. (2014). Influence of functional groups on organic aerosol cloud condensation nucleus activity. *Environmental Science & Technology*, *48*(17), 10182–10190. https://doi.org/10.1021/es502147y

Tandon, A., Rothfuss, N. E., & Petters, M. D. (2019). The effect of hydrophobic glassy organic material on the cloud condensation nuclei activity of particles with different morphologies. *Atmospheric Chemistry and Physics*, *19*(5), 3325–3339. https://doi.org/10.5194/acp-19-3325-2019

Twohy, C. H., & Poellot, M. R. (2005). Chemical characteristics of ice residual nuclei in anvil cirrus clouds: Evidence for homogeneous and heterogeneous ice formation. *Atmospheric Chemistry and Physics*, *5*(8), 2289–2297. https://doi.org/10.5194/acp-5-2289-2005

Vali, G., DeMott, P. J., Möhler, O., & Whale, T. F. (2015). Technical note: A proposal for ice nucleation terminology. *Atmospheric Chemistry and Physics*, *15*(18), 10263–10270. https://doi.org/10.5194/acp-15-10263-2015

Wagner, R., Höhler, K., Huang, W., Kiselev, A., Möhler, O., Mohr, C., et al. (2017). Heterogeneous ice nucleation of α-pinene SOA particles before and after ice cloud processing. *Journal of Geophysical Research: Atmospheres*, *122*(9), 4924–4943. https://doi.org/10.1002/2016JD026401

Wagner, R., Möhler, O., Saathoff, H., Schnaiter, M., & Leisner, T. (2010). High variability of the heterogeneous ice nucleation potential of oxalic acid dihydrate and sodium oxalate. *Atmospheric Chemistry and Physics*, *10*(16), 7617–7641. https://doi.org/10.5194/acp-10-7617-2010

Wagner, R., Möhler, O., Saathoff, H., Schnaiter, M., Skrotzki, J., Leisner, T., et al. (2012). Ice cloud processing of ultra-viscous/glassy aerosol particles leads to enhanced ice nucleation ability. *Atmospheric Chemistry and Physics*, *12*(18), 8589–8610. https://doi.org/10.5194/acp-12-8589-2012

Wang, B., Lambe, A. T., Massoli, P., Onasch, T. B., Davidovits, P., Worsnop, D. R., & Knopf, D. A. (2012). The deposition ice nucleation and immersion freezing potential of amorphous secondary organic aerosol: Pathways for ice and mixed-phase cloud formation. *Journal of Geophysical Research*, *117*(D16), D16209. https://doi.org/10.1029/2012JD018063

Wehner, B., Philippin, S., & Wiedensohler, A. (2002). Design and calibration of a thermodenuder with an improved heating unit to measure the size-dependent volatile fraction of aerosol particles. *Journal of Aerosol Science*, *33*(7), 1087–1093. https://doi.org/10.1016/S0021-8502(02)00056-3

Welti, A., Lüönd, F., Stetzer, O., & Lohmann, U. (2009). Influence of particle size on the ice nucleating ability of mineral dusts. *Atmospheric Chemistry and Physics*, *9*(18), 6705–6715. https://doi.org/10.5194/acp-9-6705-2009

Wilson, T. W., Murray, B. J., Wagner, R., Möhler, O., Saathoff, H., Schnaiter, M., et al. (2012). Glassy aerosols with a range of compositions nucleate ice heterogeneously at cirrus temperatures. *Atmospheric Chemistry and Physics*, *12*(18), 8611–8632. https://doi.org/10.5194/acp-12-8611-2012

Wolf, M. J., Zhang, Y., Zawadowicz, M. A., Goodell, M., Froyd, K., Freney, E., et al. (2020). A biogenic secondary organic aerosol source of cirrus ice nucleating particles. *Nature Communications*, *11*(1), 4834. https://doi.org/10.1038/s41467-020-18424-6

Wong, J. P. S., Lee, A. K. Y., & Abbatt, J. P. D. (2015). Impacts of sulfate seed acidity and water content on isoprene secondary organic aerosol formation. *Environmental Science & Technology*, *49*(22), 13215–13221. https://doi.org/10.1021/acs.est.5b02686

Wright, T. P., Song, C., Sears, S., & Petters, M. D. (2016). Thermodynamic and kinetic behavior of glycerol aerosol. *Aerosol Science and Technology*, *50*(12), 1385–1396. https://doi.org/10.1080/02786826.2016.1245405

Zhang, C., Zhang, Y., Wolf, M. J., Nichman, L., Shen, C., Onasch, T. B., et al. (2020). The effects of morphology, mobility size, and secondary organic aerosol (SOA) material coating on the ice nucleation activity of black carbon in the cirrus regime. *Atmospheric Chemistry and Physics*, *20*(22), 13957–13984. https://doi.org/10.5194/acp-20-13957-2020